

CHARLES UNIVERSITY

Faculty of Science

Department of Physical and Macromolecular Chemistry

---



Bc. Alžbeta Runová

**Entropically driven cascade hybridization reactions  
for detection of microRNA**

Master's thesis - Biophysical chemistry study program

Supervisor: Mgr. Petr Cígler, Ph.D.

Prague 2020

## **PROHLÁŠENÍ**

Prohlašuji, že jsem tuto magisterskou práci vypracovala samostatně pod vedením školitele Mgr. Petra Cíglera, Ph.D. a že jsem uvedla všechny použité informační zdroje a literaturu. Tato práce ani její podstatná část nebyla předložena k získání jiného nebo stejného akademického titulu.

V Praze dne 21. 7. 2020

---

Podpis

# ACKNOWLEDGMENTS

I would like to express my very great appreciation and gratitude to my supervisor, Petr Cígler, for his valuable and constructive advice and suggestions, for his extensive knowledge shared throughout my research work, for his friendly approach, which was highly appreciated, for his optimism and motivation and of course for giving me the opportunity to work with his team.

I am particularly grateful for the assistance and mentoring of Marek Kindermann, who accompanied me throughout all my thesis research, for his endless patience, detailed explanations and in-depth knowledge, especially in physics.

I would like to offer my special thanks to Jiří Schimer for his precious help, advice, suggestions, support and everyday motivation, especially towards the end of my MSc. studies.

My sincere acknowledgements also extend to Helena Raabová, who recorded and analyzed all TEM images during my thesis research.

I would like to express my deep gratitude to Carlos Henrique Vieira Melo for proofreading my thesis.

I would like to thank all members of the Synthetic nanochemistry group for the great atmosphere, support, valuable advice and enriching coffee breaks.

This work was supported by Neuron Impuls project „Visualization of the invisible – a novel way to detection of individual miRNA molecules in living cells“ (to Petr Cígler) and by Foundation “Nadání Josefa, Marie a Zdenky Hlávkových“ (to Alžbeta Runová).

Special thanks to my Vojtěch for being so supportive and for cheering me up through the busiest and most stressful times.

Finally, I wish to thank my family, especially my parents and sisters, for their great encouragement, love, and support, throughout my whole life. None of my accomplishments would be possible without them!

# ABSTRACT

The emerging potential of miRNA molecules as diagnostic biomarkers calls for the development of a new quantification method. Current approaches usually require time-consuming and costly miRNA isolation for proper sample analysis. In this thesis, a new, isolation-free, oligonucleotide-modified gold nanoparticle (AuNP/DNA) system is proposed and designed for miRNA detection and quantification in living cells. This cascade, entropy-driven, and enzyme-free amplification system provides fluorescence signal upon selective interaction with the target miRNA. For this purpose, citrate-stabilized gold nanoparticles were synthesized, and their diameters were determined by dynamic light scattering and transmission electron microscopy. The AuNP/DNA conjugates were prepared following a recently published “freezing method”. Their reaction kinetics with the target miRNA and selectivity to various miRNAs were compared with those of an analogous DNA system without AuNPs in a series of fluorescence measurements. Furthermore, stability experiments in glutathione environment were conducted, as well as DNA electrophoresis, demonstrating the mechanistic aspects of the reaction. The reaction yields and selectivity to target miRNA of 42.31 ± 2.91 nm AuNP/DNA constructs, containing approximately 25 DNA complexes per AuNP, were up to 2 times higher than those of an analogous DNA system. Additionally, AuNP/DNA constructs showed sufficient stability in glutathione solutions up to 6 mM in concentration. Fluorescence measurements confirmed the functionality of our AuNP/DNA system and support the hypothesis that AuNP/DNA system provides faster miRNA detection than an analogous DNA system without AuNPs.

## Key words

microRNA, detection, hybridization reaction, cascade reaction, fluorescence

# ABSTRAKT

Rostoucí význam miRNA molekul jakožto diagnostických biomarkerů vyvolává poptávku po vývoji nových kvantifikačních metod. Současné přístupy umožňující její kvantifikaci zpravidla vyžadují časově náročnou a nákladnou izolaci miRNA. V této práci navrhujeme nový detekční systém založený na zlatých nanočásticích modifikovaných oligonukleotidy (AuNP/DNA), který by mohl umožnit detekci a kvantifikaci miRNA v živých buňkách bez potřeby předchozí izolace. Tento kaskádový, entropicky řízený amplifikační systém poskytuje fluorescenční signál díky přítomnosti cílové miRNA. V této práci byla velikost citrátem stabilizovaných zlatých nanočástic stanovena dynamickým rozptylem světla a transmisní elektronovou mikroskopií. Povrchová modifikace AuNP byla provedena podle nedávno publikované „vymrazovací metody“ a nanočásticový systém (AuNP/DNA) byl porovnán s analogickým DNA systémem bez přítomnosti AuNP v sérii fluorescenčních měření ukazujících kinetiku reakce a selektivitu k různým miRNA. Dále byly provedeny stabilitní experimenty v prostředí glutathionu a také DNA elektroforéza demonstrující složení vzorku během reakce.  $42.31 \pm 2.91$  nm AuNP/DNA konstrukty průměrně obsahující 25 komplexů DNA na jednu zlatou nanočástici, vykazují v porovnání s analogickým DNA systémem až dvojnásobné reakční výtěžky a vyšší selektivitu k cílové miRNA. AuNP/DNA konstrukty navíc vykazují dostatečnou stabilitu i v 6 mM glutathionu. Měření fluorescence potvrzuje funkčnost navrhovaného AuNP/DNA systému a podporuje vstupní hypotézu, že tento systém poskytuje rychlejší detekci miRNA než analogický DNA systém bez zlatých nanočástic.

## Klíčová slova

mikroRNA, detekce, hybridizační reakce, kaskádové reakce, fluorescence

# CONTENT

ABSTRACT.....	4
ABSTRAKT .....	5
1 INTRODUCTION.....	10
2 THEORETICAL PART .....	11
2.1 MiRNA.....	11
2.2 DNA nanotechnology.....	12
2.3 Hybridization.....	12
2.4 Nucleic acid structure-based amplification techniques.....	14
2.5 TMSD systems .....	17
2.6 EDC systems .....	18
2.7 Gold nanoparticles .....	20
2.8 Cellular uptake and internalization of AuNPs .....	21
2.9 Oligonucleotide-modified AuNPs.....	23
2.9.1 Oligonucleotide-modified AuNPs for RNA detection.....	24
3 AIM OF THE WORK .....	25
3.1 Particular tasks .....	25
3.2 Hypotheses .....	25
4 DESIGN OF THE DETECTION SYSTEMS .....	26
5 MATERIALS AND METHODS .....	29
5.1 Chemicals.....	29
5.2 Instruments and used software .....	30
5.3 Other materials .....	30
5.4 Methods.....	31
5.4.1 Synthesis of gold nanoparticles .....	31
5.4.2 Transmission electron microscopy .....	31

5.4.3	Dynamic light scattering.....	32
5.4.4	Determination of the concentration of gold nanoparticles.....	32
5.4.5	Synthesis of oligonucleotide-modified gold nanoparticles.....	33
5.4.6	Determination of the amount of DNAs on the surface of gold nanoparticles	33
5.4.7	Fluorescence measurements .....	34
5.4.7.1	Sample composition.....	35
5.4.8	Stability of AuNP/DNA conjugates in glutathione.....	36
5.4.9	DNA polyacrylamide gel electrophoresis.....	37
6	RESULTS.....	38
6.1	Synthesis and characterization of gold nanoparticles .....	38
6.1.1	Determination of the size of gold nanoparticles .....	38
6.2	Construction and characterization of oligonucleotide-modified gold nanoparticles... ..	40
6.2.1	Determination of the number of DNA complexes per gold nanoparticle.....	40
6.2.2	Comparison of reaction yields for AuNPs with different DNA coverage density.....	42
6.3	Measurements of the progress of the reaction.....	43
6.3.1	Selectivity to various miRNAs .....	45
6.4	Stability of AuNP/DNA in GSH environment.....	45
6.5	Reaction mixture composition (DNA electrophoresis).....	46
7	DISCUSSION.....	48
8	CONCLUSION .....	52
9	SUPPLEMENTS .....	53
	S1 Determination of the concentration of gold nanoparticles .....	53
	S2 Calibration curve for DNA1a and DNA2a.....	53
	S3 Comparison of AuNP/DNA and AuNP size .....	55
	S4 Stability of AuNP/DNA complex in reaction medium .....	55
10	REFERENCES .....	57

## LIST OF ABBREVIATIONS

AuNP	gold nanoparticle
DLS	dynamic light scattering
DNA	deoxyribonucleic acid
EDC	entropy-driven catalysis
EDRE	entropy-driven RNA explorer
FRET	Förster resonance energy transfer
GSH	glutathione
HCR	hybridization chain reaction
CHA	catalytic hairpin assembly
IEL	intuitive energy landscape
lncRNA PCA3	long noncoding RNA of prostate cancer gene 3
miRNA	micro ribonucleic acid
mRNA	messenger ribonucleic acid
NN model	nearest-neighbour model
PBS	phosphate-buffered saline
QD	quantum dot
RFU	relative fluorescence unit
RME	receptor-mediated endocytosis
RNA	ribonucleic acid
RP	radiating plasmon
RT	room temperature
RT-qPCR	quantitative reverse-transcription polymerase chain reaction
SDA	strand displacement amplification
TBE	tris-borate-EDTA buffer
ssDNA	single-stranded deoxyribonucleic acid

ssRNA	single-stranded ribonucleic acid
TEM	transmission electron microscopy
TMSD	toehold-mediated strand displacement

# 1 INTRODUCTION

MiRNAs are short, non-coding RNA molecules. These post-transcriptional regulators of gene expression play a key role in several cellular processes. Furthermore, abnormal miRNA expression levels are associated with various human diseases, thus implying that miRNAs may be used as both diagnostic biomarkers and drug targets<sup>1</sup>. As such, direct miRNA imaging in living cells may be a valuable tool for cancer detection and drug efficacy evaluation. In this context, DNA nanotechnology provides therefore a promising new approach for miRNA visualization in living cells.

Several physical properties of DNA enable its use as a functional material for the construction of DNA nanostructures. Automated synthesis of oligomers with possibility of modification with fluorescent dyes facilitates the use of DNA conjugates as detection tools. AuNP/DNA conjugates combine the chemical and structural properties of DNA with the physicochemical properties of AuNPs. AuNPs are chemically stable particles with unique optical and electronic properties and high biocompatibility and are thus ideal materials for nanotechnology<sup>2</sup>.

This thesis focuses on the synthesis of AuNP/DNA conjugates for their use as miRNA detection tools. The system applies an enzyme-free structure-based amplification technique known as toehold-mediated strand displacement to produce detectable fluorescence signal in the presence of miRNAs. The aim of the work is to highlight the advantages of the AuNP/DNA system over an analogous DNA system. Moreover, these AuNP/DNA conjugates will be further evaluated *in vitro* for their possible application as fluorescence imaging probes in diagnostics.

## 2 THEORETICAL PART

### 2.1 MiRNA

MicroRNAs are short, approximately 20-nucleotide-long, noncoding, evolutionarily conserved RNAs, which are encoded in almost all eukaryotes. MiRNAs are implicated in various physiological processes such as development, differentiation, growth and metabolism through post-transcriptional regulation of gene expression<sup>3</sup>.

Deficiencies or excesses of different miRNAs have been associated with a number of diseases, ranging from cardiovascular, neurodevelopmental, autoimmune, and skin diseases to cancer<sup>4</sup>. For this reason, the determination of miRNA expression levels is a critical step in methods involving diagnostic markers for cancer and other diseases.

Several methods for the detection of individual miRNAs are currently available, including northern blotting, quantitative reverse-transcription polymerase chain reaction (qRT-PCR), in situ hybridization, microarray profiling, or next-generation sequencing (Figure 1)<sup>5</sup>. However, all of these methods have some disadvantages, such as high cost, low sensitivity and selectivity, the need for miRNA extraction, and incompatibility with living cells. To overcome these drawbacks, a new amplification method must be developed for the detection and accurate quantification of miRNA in living cells at a single-molecule level, and DNA nanotechnology may provide a promising new approach.

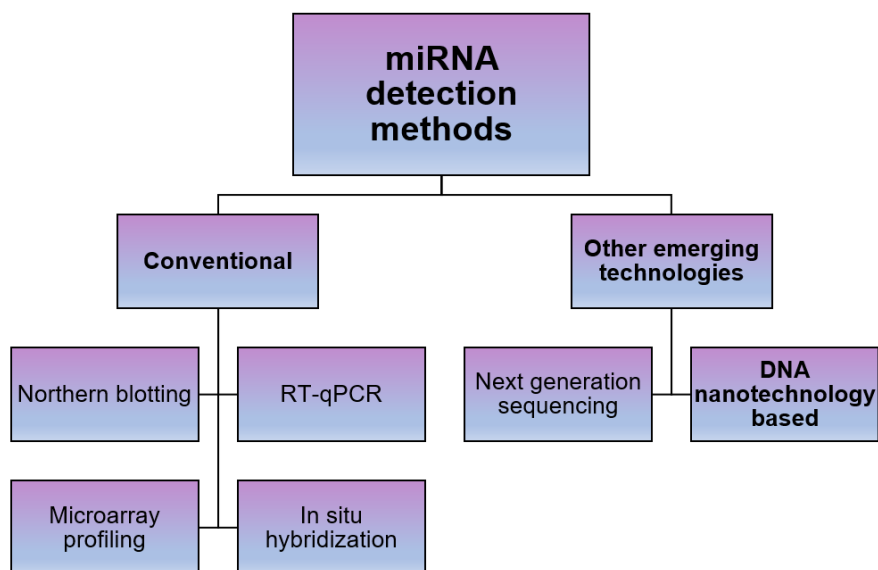


Figure 1 Representation of various miRNA detection techniques.

## 2.2 DNA nanotechnology

DNA nanotechnology makes use of the properties of DNA, as well as RNA and other synthetic nucleic acid analogs. As versatile biomaterials, nucleic acids can be used to construct various nanodevices used for sensing, targeting, delivery and therapy, among other purposes<sup>6</sup>.

DNA is well-suited for designing precise structures with arbitrary control over their size and shape. In aqueous solution, two nucleic acid strands spontaneously self-assemble into the double helix structure, following the Watson-Crick base pairing rules. This sequence-dependent and highly selective hybridization process allows the construction of DNA duplexes, which can be modeled into the requested target structures<sup>7</sup>.

## 2.3 Hybridization

The formation of a duplex from two strands of DNA or RNA through hybridization can be simplistically regarded as a bimolecular reaction with a rate constant  $k_{\text{hyb}}$ . The reverse reaction can be viewed as a unimolecular reaction with rate constant  $k_{\text{dis}}$ . After some time, an equilibrium between these two reactions is reached, which can be described as:



where A and B represent individual strands and AB the formed duplex structure. The system is considered a two-state system, wherein DNA or RNA strands are either fully dissociated or fully associated<sup>6</sup>.

The equilibrium constant K of the reaction is given by the relation:

$$K = \frac{c_{AB}c_{st}}{c_A c_B}, \quad \text{Eq. 2}$$

where  $c$  represents equilibrium molar concentration of the reactants A and B, and the product of the reaction AB; and  $c_{st}$  the standard molar concentration. *Eq. 2* applies for diluted solutions where the activity coefficient of DNAs is close to 1<sup>8</sup>.

The equilibrium constant is related to the standard molar free energy of reaction ( $\Delta_r G^\ominus$ ) by:

$$\Delta_r G^\ominus = -RT \ln(K), \quad \text{Eq. 3}$$

where  $T$  denotes thermodynamic temperature and  $R$  gas constant. The standard molar free energy of reaction depends only on temperature and the choice of standard states of the reactants and products<sup>8</sup>.

The relation which connects the standard molar free energy of reaction with the standard molar reaction enthalpy ( $\Delta_r H^\ominus$ ) and standard molar reaction entropy ( $\Delta_r S^\ominus$ ) is described as<sup>8</sup>:

$$\Delta_r G^\ominus = \Delta_r H^\ominus - T \Delta_r S^\ominus. \quad \text{Eq. 4}$$

Entropy, which can be described as a measure of disorder, changes during the process of hybridization, as we obtain one duplex from two oligonucleotides. Furthermore, solvent molecules and other components of the solution bind in a different manner to random coils than to duplexes<sup>6</sup>.

An important source of change in enthalpy during hybridization comes from the stacking interactions between neighboring nucleotides of single strands<sup>9</sup>.

When describing DNA hybridization, the melting temperature,  $T_M$ , is an important parameter to consider.  $T_M$  is a temperature at which one half of DNA strands are present in double-helical structure, whereas the other half has a random-coiled structure. The melting temperature of a duplex can be predicted when its thermodynamic parameters are known. The nearest-neighbor (NN) model makes it possible to estimate these parameters. The relation of  $T_M$  for non-self-complementary molecules with the standard enthalpy,  $\Delta H^\ominus$ , and entropy,  $\Delta S^\ominus$ , is described as:

$$T_M = \frac{\Delta H^\ominus}{\Delta S^\ominus + R \ln\left(\frac{c_T}{4}\right)}, \quad \text{Eq. 5}$$

where  $c_T$  denotes the total oligonucleotide concentration. The melting temperature is not a constant value; it is markedly dependent on the oligonucleotide concentration and on the environment in which hybridization occurs<sup>10</sup>.

The NN model anticipates the formation energy of all possible secondary structures that can be formed from a given sequence. The NN model conjectures that the stability of a specific base pair relies on the type and mutual orientation of neighboring base pairs<sup>11</sup>. The standard free energy of nucleic acid duplex formation,  $\Delta G_i^\ominus(\text{total})$ , at 37 °C is represented by:

$$\Delta G_i^\ominus(\text{total}) = \Delta G_i^\ominus(\text{init}) + \Delta G_i^\ominus(\text{sym}) + \sum_j n_{ij} \Delta G_j^\ominus, \quad \text{Eq. 6}$$

where  $i$  denotes each different oligonucleotide duplex,  $\Delta G_j^\ominus$  represents standard free energies for the 10 possible Watson-Crick nearest neighbor stacking interactions and  $n_{ij}$  the number of occurrences of each nearest neighbor,  $j$ , in each sequence,  $i$ . The term  $\Delta G_i^\ominus(\text{init})$  is the initiation standard free energy and  $\Delta G_i^\ominus(\text{sym})$  refers to the self-complementarity of the duplex and equals zero for non-self-complementary molecules<sup>10</sup>.

## 2.4 Nucleic acid structure-based amplification techniques

Functional nucleic acid structure-based amplification techniques have become very attractive in the field of biotechnology. They can be divided into two categories: thermocycling and isothermal amplification techniques (see *Figure 2*). In contrast to thermocycling amplification techniques, isothermal amplification protocols can be performed under simple conditions (constant temperature). Isothermal amplification techniques include strand displacement amplification (SDA), such as toehold-mediated strand displacement (TMSD), which represents one of the most popular isothermal amplification strategies<sup>12</sup>. It deviates from the traditional view of catalysis in biological organisms in that it is enzyme-free and does not alter covalent bonds<sup>13</sup>.

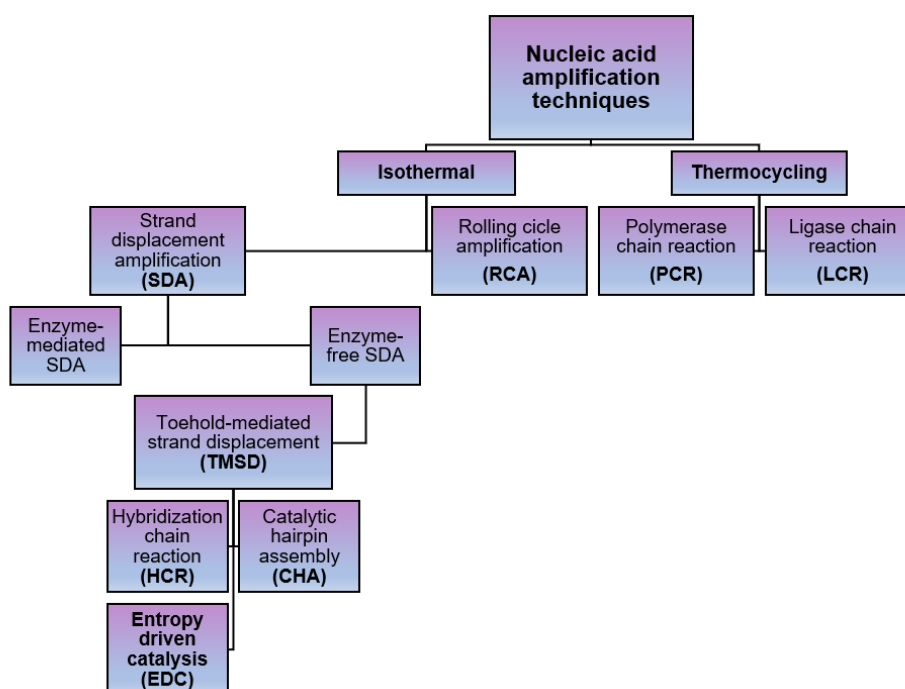
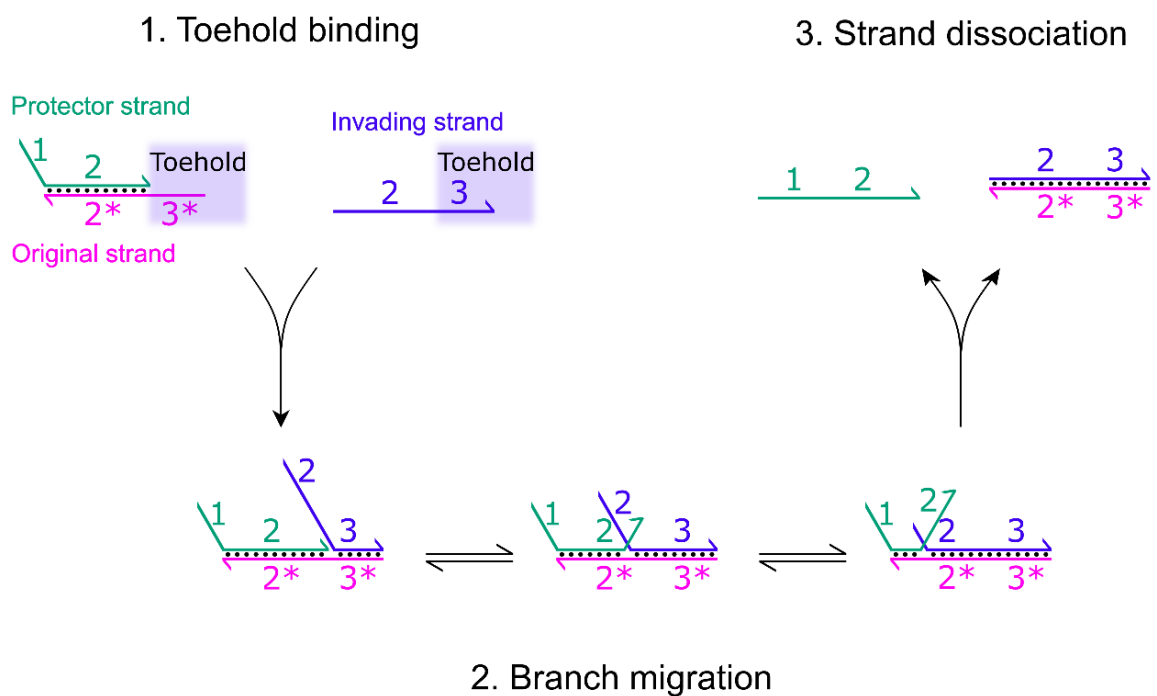


Figure 2 Representation of nucleic acid structure-based amplification techniques.

TMSD makes it possible to exchange one strand of DNA or RNA in double-stranded structure for another, invading strand through branch migration (see *Figure 3*). Branch migration is the movement of the point at which two homologous DNA molecules exchange base-paired strands<sup>14</sup>. The rate of this random walk process depends on the length of the branch migration section<sup>15</sup>. Toehold is an overhanging sequence in a double-stranded structure which initiates the process of TMSD through hybridization with the invading strand. As the total amount of base pairs in the reactants and products does not change, the reaction is driven forward thermodynamically by the entropic gain of the liberated molecules<sup>13</sup>.



*Figure 3 Representation of the process of TMSD. TMSD starts with a double-stranded DNA structure containing an original strand and a protector strand. The original strand contains the toehold domain which is complementary to the invading strand, a sequence of ssDNA or ssRNA complementary to the original strand. The process is triggered by hybridization of the invading strand with the toehold domain. This initial hybridization step is rate limiting and can be regulated by varying the length and the sequence composition of the toehold domain<sup>16</sup>. Binding of the invading strand triggers branch migration which results in displacement of the protector strand containing less complementary base pairs with the original strand than the invading strand. Adapted from <sup>17</sup>.*

To understand the biophysics of TMSD, an intuitive energy landscape (IEL) model can be used to predict the kinetics and thermodynamics of the process<sup>18</sup>. *Figure 4* describes the state space of the IEL.

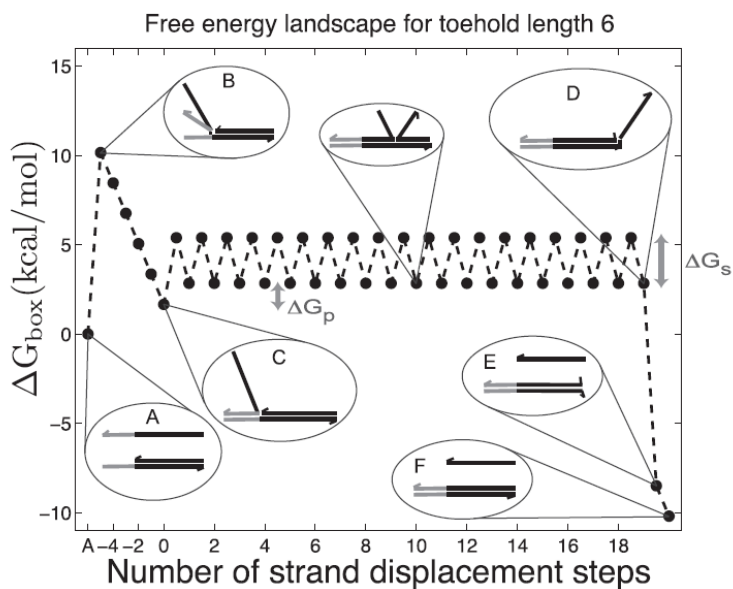


*Figure 4* Representation of the free energy of the virtual box ( $\Delta G_{\text{box}}$ ) relative to state A modeled by the IEL at 25°C for a six base toehold<sup>18</sup>.

State A represents a distinct invader strand and a complex of the original and protector strand<sup>18</sup>. State B corresponds to the formation of a first base pair between the invader strand and the toehold region of the original strand. This initial binding causes a rise in the free energy attributable to the reduction in the entropy of the system. Formation of every additional toehold base pair is described by a new state with state C having all the toehold base pairs formed. Each step of branch migration causes the replacement of the protector-original strand base pair by the invader-original strand base pair during which the system has to get through an effective transition state of raised free energy (represented by  $\Delta G_s$ ).  $\Delta G_p$  represents possible changes in the free energy of the intermediates of branch migration due to structural differences of the branch migration junction. The branch migration results in the spontaneous displacement of the protector strand represented by state E, followed by the formation of the last base pair between the invader and original strand (state F)<sup>18</sup>.

The toehold represents a key domain controlling both the kinetics and thermodynamics of the process of strand displacement. Even if the reverse reaction can occur, its rate is six orders of magnitude slower, which renders the TMSD reaction

practically irreversible<sup>15</sup>. Two factors elucidate the reliance of TMSD kinetics on toehold length. First, a single step of branch migration is considerably slower than a dissociation of a single base pair as every branch migration step disrupts favorable stacking interactions and causes greater structural rearrangement. Second, the initiation of branch migration is slower than the process itself as the initiation engenders a thermodynamic penalty which arises from the steric hindrance of the single-stranded overhangs and duplexes at the branch migration junction, disruption of stacking interactions, and decrease of conformational freedom. TMSD with RNA structures is expected to have similar kinetics even though the strand displacement rates are significantly slower while the base pairing energy is generally stronger<sup>18</sup>.

## 2.5 TMSD systems

DNA circuits based on DNA hybridization are mostly engineered to provide an enzyme-free amplification. The vast majority of DNA circuits are powered by the TMSD. The thermodynamics of the overall process is driven by enthalpic and/or entropic considerations. More common enthalpic gain is obtained from the free energy originating from toehold binding. More unique entropic gain is achieved whereas one input strand releases two or more output strands<sup>15</sup>.

Among the TMSD systems, catalytic hairpin assembly (CHA) and hybridization chain reaction (HCR) are techniques which use DNA hairpins. These single-stranded loops make toeholds, due to steric constraints, unavailable for hybridization until the hairpin is opened<sup>6</sup>. In the CHA, as well as in the HCR, an initiator triggers a cascade of hybridization reactions between two DNA hairpins, leading to the formation of multiple duplexes (CHA) or a nicked double helix with many repeated units (HCR)<sup>12</sup>. These outputs can be coupled to several analytical methods<sup>19</sup>. However, these methods also have some weaknesses, which may cause high background or false-positive signals. For example, in CHA, the two hairpin structures can interact non-specifically, even in the absence of the initiator of the process, which increases the background level<sup>20</sup>.

In contrast to the CHA and the HCR, which are driven by enthalpic and entropic factors, entropy-driven catalysis (EDC) is generally controlled by the overall entropy of the mechanism<sup>19</sup>. The process is triggered by hybridization of the input strand (invading strand) with the toehold domain, which results in the release of the first output strand.

This exposes another toehold domain to which the fuel strand binds and displaces the second output strand. The fuel also releases the input strand which results in the formation of a double-stranded waste product that does not further interact<sup>13</sup>. While the overall number of base pairs throughout the process is unchanged, one input strand releases much more output strands, and thus the whole process is driven by the increase in the entropy of the system<sup>19</sup>. This design is simpler, faster and more stable than systems based on hairpin structures, which may cause high background leakage from interactions between complicated secondary structures<sup>21</sup>.

## 2.6 EDC systems

EDC systems provide an attractive tool for construction of different DNA nanodevices used for detection of various target molecules. In the section below, some of these systems, predominantly used for miRNA detection, are described.

In 2015, Lv et al. engineered an enzyme-free DNA amplification system with flexible sequence design based on EDC, called Ebeacon. Ebeacon system includes a target structure, fuel and ternary beacon complex containing fluorescent dye and quencher. The entire amplification cycle is triggered by the addition of a target structure which initiates the process of TMSD, resulting in the displacement of fluorophore-labelled DNA<sup>22</sup>.

Eckhoff et al. engineered a catalytic cascade system by coupling an entropy-driven DNA circuit with deoxyribozyme catalysis. A specific sequence triggers the process of TMSD, which leads to the release of an amplified invader strand that displaces DNAzyme present in a duplex structure. DNAzyme subsequently undergo a conformational change into an active G-quadruplex form that oxidizes the colorless substrate into a green product<sup>23</sup>.

In 2018, Tan et al. have engineered an entropy-driven 3D DNA amplifier that makes it possible to detect intracellular mRNAs in living cells. The system consists of two modules – the entropy beacon tetrahedron module containing DNAs modified with a fluorescent dye and a quencher, and the fuel tetrahedron module. The presence of target mRNA triggers a cascade of strand displacement reactions resulting in the release of labelled DNA which can provide fluorescence signal. The recovery of the target miRNA allows for multiple turnover<sup>24</sup>.

The long, noncoding RNA of prostate cancer gene 3 (lncRNA PCA3) can be visualized in living cells using TAT peptide-functionalized titanium carbide MXenes modified with an entropy-driven RNA explorer (EDRE). In cells, TAT peptide and EDRE are released by the glutathione-triggered cleavage followed by TAT-guided delivery of EDRE into the nucleus, where the lncRNA PCA3 initiates the process of TMSD, resulting in the release of the fluorophore-labelled DNA that provides the fluorescence signal<sup>25</sup>.

In 2017, Ou et al. developed a miRNA detection assay based on EDC utilizable in a complex sample matrix. The system consists of a hairpin template, a ternary DNA complex, a fuel strand, and a polymerase and nicking endonuclease. The presence of the target miRNA, which binds to the loop of the hairpin template, causes an extension of the template catalyzed by the polymerase. The polymerization process creates the recognition site for the nicking endonuclease, which cleaves one strand of DNA known as the trigger strand. The process is followed by a strand displacement synthesis that extends the 3'-end at the nick, which displaces the DNA trigger strand. This cycling process of polymerization and cleavage produces several trigger strands. The produced trigger strand initiates the process of TMSD by binding to the ternary DNA complex containing a fluorescent dye and a quencher. The fluorophore and the trigger are released, which allows the trigger to be reused. One trigger strand can release multiple fluorophore-labelled strands, so the fluorescence signal is significantly amplified<sup>26</sup>.

In 2016, Ma et al. showed that cancer-related miRNAs can be detected in living cells using AuNPs modified with quantum dots (QDs) through DNA linker<sup>27</sup>. AuNP serves as a quencher of fluorescence of QDs. In the presence of the single-target miRNA, multiple QDs are released through the process of TMSD with the help of fuel DNA, resulting in amplified fluorescence.

In 2017, a DNA nanomachine used for intracellular miRNA imaging was constructed by Liang et al. The nanomachine consists of an AuNP covered with DNA substrates containing fluorophores and an affinity ligand, a walking leg, and a fuel. The presence of the target miRNA drives the walking leg and triggers the TMSD process that releases the fluorophore-labelled DNAs recovering previously quenched fluorescence signal<sup>21</sup>.

As discussed above, some of these nanomachines consist of nanoparticles, which make it possible to group a large number of substrates together. In addition, because DNAs designed for nanomachine construction are often modified with fluorophores, AuNPs can be used for their capacity to quench the fluorescence of all the substrates present on their

surface, when placed at a right distance from the surface, thereby avoiding the use of intramolecular quenchers, which render the synthesis of such structures very expensive.

## 2.7 Gold nanoparticles

Gold nanoparticles are suitable for biological applications – they are chemically inert and can be easily modified. Additionally, they can be used as effective fluorescence quenchers.

Fluorescence quenching generally occurs by contact quenching or Förster resonance energy transfer (FRET) quenching. In contact quenching, the close proximity between fluorophore and quencher allows the direct electronic interaction between the excited state of the fluorophore and the quencher. As a result, light absorbed by the fluorophore is non-radiatively transferred as heat to the surrounding environment, while a little amount of energy is released radiatively<sup>28</sup>. FRET quenching is based on a dipole-dipole interaction between a fluorophore in the excited state and an acceptor. Quenching efficiency depends on several factors and properties of the donor and the acceptor and, importantly, on the inverse sixth power of the distance between them and is thus significant over a very short distance range of 2-10 nm<sup>29</sup>.

The fluorophore in the excited state acts as an oscillating dipole that can induce oscillations of the electrons in the metal. The electric field produced by the metal is affected by interactions of the incident light with the metal surface and by interaction of the fluorophore oscillating dipole with the metal. This field can interact with the excited fluorophore and modify its emission<sup>30</sup>. There are two main factors affecting the changes in fluorescence caused by metal nanoparticles. First, the plasmon field around the gold nanoparticle generated by the incident light increases the excitation decay rate of the fluorophore resulting in fluorescence emission enhancement. Second, the dipole energy around the particle decreases the radiative to non-radiative decay rate ratio and the quantum yield of the fluorophore, which results in fluorescence quenching. The effect of the metal on fluorophore emission depends on the particle size and shape, on surface modification, on the wavelength of the incident light, on the distance between the fluorophore and the nanoparticle surface, on the orientation of the fluorophore towards the nanoparticle, and on their spectral overlap<sup>31</sup>. *Figure 5* shows the changes in quantum efficiency of the fluorophore according to various factors.

The radiating plasmon (RP) model explains the effect of the metal nanoparticle on the fluorophore predominantly based on the size of the nanoparticle and on the distance between the nanoparticle and the fluorophore. This model makes it possible to predict fluorescence enhancement or fluorophore quenching near the metal nanoparticle by semi-classical electrodynamics. The RP model suggests that AuNPs with diameter below 40 nm are more efficient quenchers of fluorescence than larger AuNPs<sup>32</sup>.

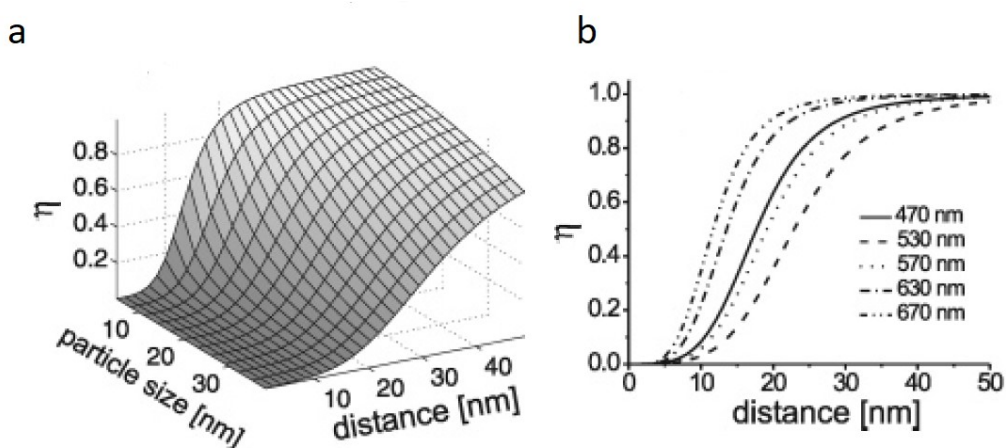


Figure 5<sup>29</sup> (a) Representation of quantum efficiency of the fluorophore at different distances from the surface of AuNPs of different diameters. (b) Representation of quantum efficiency of the fluorophore placed at different distances from 15 nm AuNP for different emission wavelengths. The quenching of the fluorophore is effective for a distance of at least 10 nm from AuNP surface for different sizes of AuNPs, as well as various emission wavelengths of the emitters.

## 2.8 Cellular uptake and internalization of AuNPs

Different types of nanoparticles display different pathways for cellular internalization. Endocytosis represents active transport of objects which are enclosed in vesicles or vacuoles formed from the cytoplasmic membrane of a cell. Endocytosis includes energy-dependent processes such as phagocytosis, pinocytosis, clathrin-dependent, and caveolae-dependent endocytosis<sup>33</sup>.

The mechanism of cellular uptake is a very complex process that depends not only on size, shape, coating, and charge of the nanoparticles but also on the purity of nanoparticles, their aggregation states, nanoparticle-protein interactions, cell types, cell

treatment, and many others<sup>33</sup>. Even though not all of these factors are dominant, for each type of nanoparticle, the process of cellular uptake is complicated and to some extent unique.

Uncoated gold nanoparticles preferentially enter cells via clathrin-dependent endocytosis, also known as receptor-mediated endocytosis (RME). During RME, receptors present on the cell membrane interact with the ligands on the nanoparticle surface. The nanoparticles are internalized by the inward budding of the plasma membrane, thereby forming clathrin-coated vesicles<sup>33</sup>.

Modification of the gold nanoparticle surface can lead to a different cellular uptake pathway as the charge, shape, and size of the nanoparticle may be changed. Coating AuNPs with oligonucleotides causes them to acquire negative charge. The interface between the nanoparticle and the surrounding environment is markedly changed, which results in different cellular uptake pathway<sup>33</sup>.

Cellular uptake is highly dependent on the density of oligonucleotide coverage on the AuNP surface. The density of oligonucleotides correlates with the number of adsorbed proteins to the DNAs on the AuNP surface upon exposure to cell culture media and provides a possible explanation for increased cellular uptake of AuNPs with higher DNA loading density as the interaction may represent a possible mechanism of recognition and subsequent internalization of the nanoparticles into the cells<sup>34</sup>.

Oligonucleotide-modified AuNPs can enter the cells through the raft-dependent endocytosis. Lipid rafts are microdomains within the membrane bilayer, rich in cholesterol and sphingolipids. These domains can internalize ligands by a process termed raft-dependent endocytosis. Caveolae are invaginations of plasma membrane rich in caveolin-1, forming a subdomain of lipid rafts. Caveolins induce the formation of invaginated caveolae but also domains that regulate the function of lipid rafts and endocytosis<sup>35</sup>.

The caveolae-mediated pathway can bypass lysosomes and thus helps to enhance the concentration of therapeutics in cells by avoiding lysosomal degradation<sup>36</sup>. This pathway characterized by clathrin-independence and sensitivity to cholesterol can be regulated by caveolin-1 and by the actin cytoskeleton<sup>35</sup>.

The cellular uptake of oligonucleotide-modified AuNPs is mediated mainly by class A scavenger receptors and by caveolae<sup>37</sup>. Upon binding to class A scavenger receptors on the cell surface, caveolins and increased levels of cholesterol induce the formation of caveolar invaginations, whose fission is subsequently mediated

by dynamin. Released caveolar vesicles, which require actin for movement within the cell, fuse with caveosomes or endosomes. Caveosome containing nanoparticles then proceed to endoplasmic reticulum, through which nanoparticles usually penetrate into the cytosol<sup>36,38</sup>.

## 2.9 Oligonucleotide-modified AuNPs

Oligonucleotide-modified gold nanoparticles stand out as promising nanomaterials for their potential therapeutic and diagnostic applications with several beneficial properties, such as higher cellular uptake, nuclease resistance, and limited immune and cellular response<sup>39</sup>.

Oligonucleotide-modified AuNPs show higher stability towards nucleases than molecular DNAs. DNA degradation can be modeled as a two-step process. At first, the enzyme associate with the substrate and then hydrolyzes the nucleic acids. Even though the association of the enzyme is more favorable for oligonucleotide-modified AuNPs, slower hydrolysis than that of molecular DNA results in enhanced nuclease resistance. The high local salt concentration, which inhibits nucleases, also enhances consequently the stability of nucleic acids present on AuNPs<sup>40</sup>.

Citrate-stabilized AuNPs, which serve as a starting material for oligonucleotide-modified AuNPs formation, show a significant cellular response caused by the instability of these particles in the cell culture medium, resulting in aggregation. Conversely, oligonucleotide-modified AuNPs cause no significant changes in gene expression, cell-cycle progression, or apoptosis induction and remain stable in cell culture medium throughout 24-hour treatment period<sup>41</sup>.

The cellular innate immune response can detect foreign nucleic acids and induce a chain of signaling events leading to cell death and activation of adaptive immune system. However, the specific architecture of oligonucleotide-modified AuNPs allows limited innate immune system activation. This is also associated with the density of oligonucleotides on AuNP surface. Lower DNA density enables more significant interaction with cellular DNA binding proteins, which detect foreign nucleic acids, and therefore higher DNA loading reduces the cellular innate immune response<sup>39</sup>.

### **2.9.1 Oligonucleotide-modified AuNPs for RNA detection**

The first attempt to synthesize oligonucleotide-modified AuNPs for visualization and quantification of RNA molecules was performed by Seferos et al.<sup>42</sup>. These nanoparticles containing fluorophore-modified oligonucleotides have many advantages, such as efficient gold quenching, cellular uptake without the use of transfection agents, enzymatic stability and many more. Moreover, these complexes display low background fluorescence and high signaling efficiency. However, one target molecule provides fluorescence signal from only one displaced fluorophore-labelled DNA<sup>42</sup>. Nevertheless, the development of such particles could lead to a unique and highly beneficial approach to RNA detection and quantification.

## **3 AIM OF THE WORK**

The goal of this thesis is to synthesize and test oligonucleotide-modified gold nanoparticles for cascade amplification of a fluorescence signal serving as a tool for miRNA detection and quantification in living cells and to compare them with an analogous structure without gold nanoparticles.

### **3.1 Particular tasks**

- Description of the detection systems
- Synthesis and characterization of AuNPs
- Synthesis and test of oligonucleotide-modified AuNPs with various DNA coverage
- Kinetic measurements and analysis of the process of release of fluorophore-labelled DNAs due to the presence of miRNA (using structure with AuNPs and structure with intramolecular quenchers)
- Measurement of sensitivity to different miRNAs (using structure with AuNPs and structure with intramolecular quenchers)
- Stability measurements in GSH environment
- Electrophoresis showing sample composition during the process of release of fluorophore-labelled DNAs

### **3.2 Hypotheses**

One of the main goals of this thesis is to test whether the process of release of fluorophore-labelled DNAs from the structure with gold nanoparticles due to the presence of miRNA would be faster than in the case of a structure with intramolecular quenchers. The gold nanoparticles make it possible to cluster a large number of substrates (ternary DNA complexes) which should increase the rate of the whole process. Additionally, the structure with gold nanoparticles does not require any supplemental transfection agents to enter the cells, which should cause less stress. Furthermore, the use of gold nanoparticles instead of intramolecular quenchers renders the synthesis of such structures much more affordable.

## 4 DESIGN OF THE DETECTION SYSTEMS

In this work, two similar systems used for miRNA detection and quantification are compared (see *Figure 6*).

The first system consisting of ternary DNA complex, contains DNA3 with 2 intramolecular quenchers and DNA1 and DNA2 with fluorescence dye - Cy3<sup>43</sup>. The second system, proposed in this work in order to find a better nanoparticle-based miRNA detection system, is analogous to the system with intramolecular quenchers. The design differs in position and type of fluorescence dyes and type of the quencher. DNA1a and DNA2a contain Atto633 at 5' end, whereas DNA1 and DNA2 include Cy3 at 3' end. Additionally, in the second system, the role of the quencher is taken over by gold nanoparticle, and thus DNA3a does not contain any intramolecular quencher. The DNA sequences for fluorophore-labelled DNAs are the same, but DNA3a contains polyT sequence and thiol group at 3' end, which makes it possible to form a covalent bond between the sulfur from the thiol group of DNA and the gold.

The mechanism of the reaction is the same for both systems. *Figure 7* shows one cycle of the reaction for system with intramolecular quenchers. The only difference is in the structure of the systems, not in the shown mechanism.

The system with gold nanoparticles provides several advantages. One of them is the fact that a large number of ternary DNA complexes is placed on one gold nanoparticle. *Figure 8* shows the principle of the reaction on gold nanoparticles. MiRNA initiates the process of strand displacement which results in release of both fluorophore-labelled DNAs that can provide fluorescence signal as they are no longer near the quencher. At the end of one cycle, miRNA is also released and already close to another ternary DNA complex, which should accelerate the overall process.

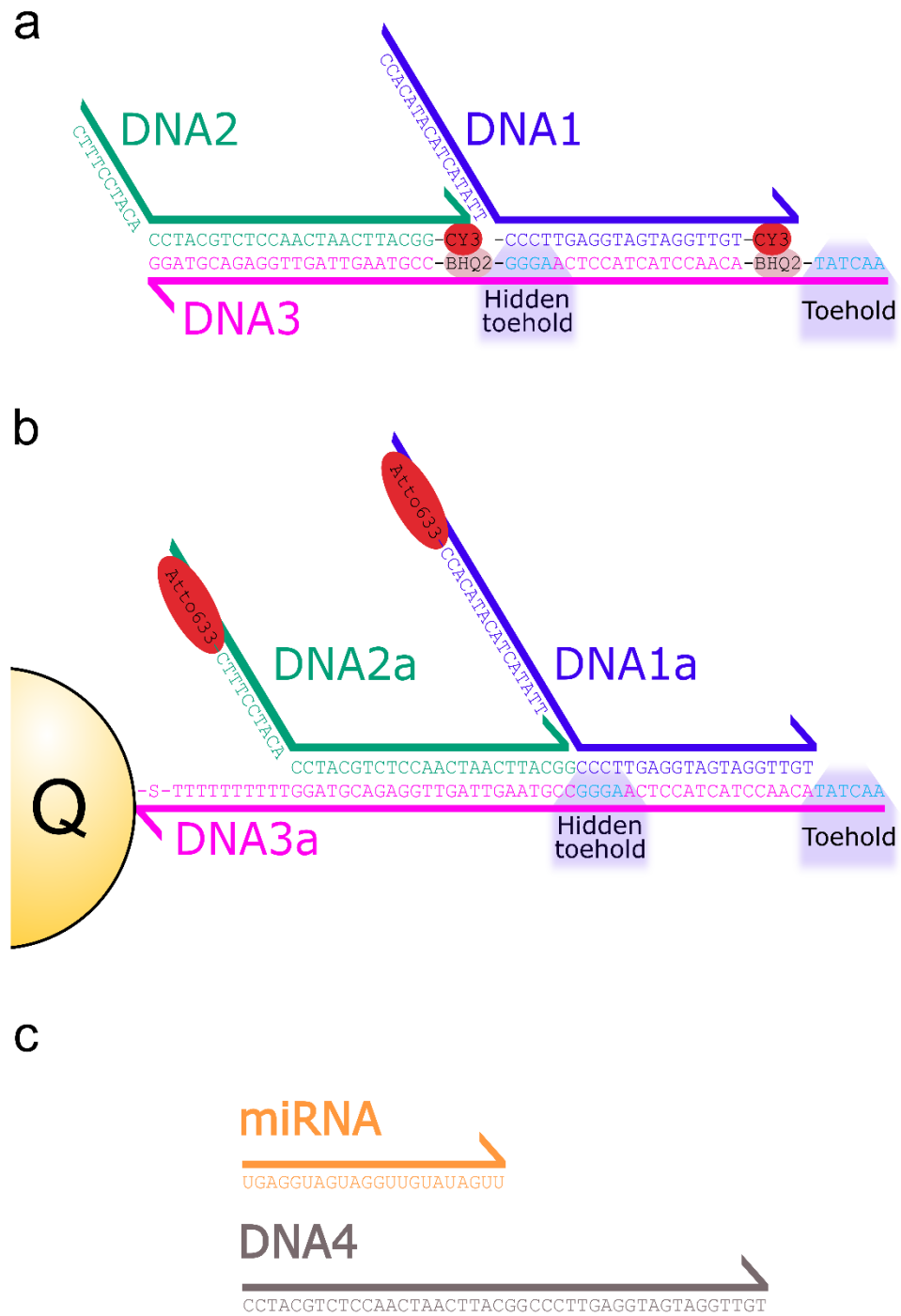


Figure 6 Representation of structures and sequences of (a) ternary DNA complex with intramolecular quenchers, (b) ternary DNA complex on AuNP and (c) sequences of DNA4 (fuel) and let-7a (miRNA). The arrows display direction of the sequence from 5' to 3' end.

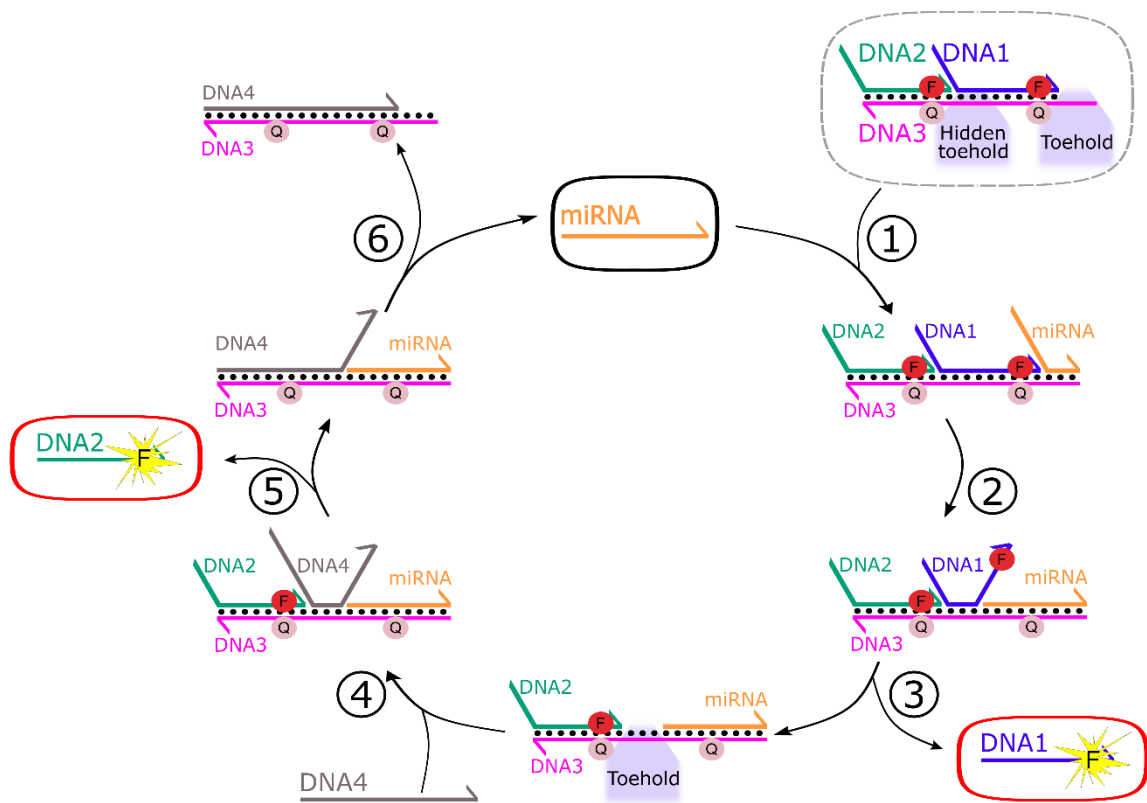


Figure 7 The mechanism of the process of detection of miRNA using the system with intramolecular quenchers. The individual steps of the process: 1. miRNA triggered TMSD; 2. Branch migration; 3. Displacement of the first fluorophore-labelled DNA; 4. DNA4 triggered TMSD; 5. Displacement of the second fluorophore-labelled DNA; 6. Release of the initiator of the reaction (miRNA).

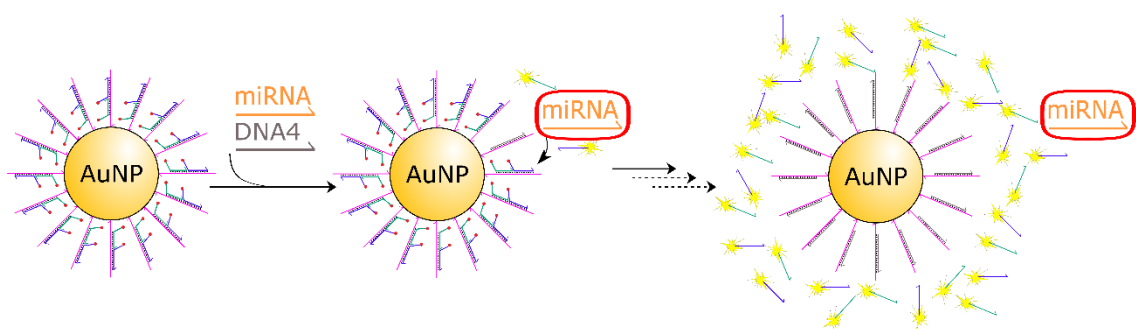


Figure 8 Principle of the reaction on gold nanoparticles.

## 5 MATERIALS AND METHODS

### 5.1 Chemicals

10 mM Tris	Qiagen, NL
Acrylamide, Electrophoresis Grade, 99+%	Alfa Aesar, US
Ammonium peroxydisulfate, Electrophoresis Grade	Alfa Aesar, US
Boric acid	SIGMA, US
DNA1, DNA1a, DNA2, DNA2a, RNA sequences	metabion international, DE
DNA3, DNA3a, DNA4	Generi Biotech, CZ
Dithiothreitol (DTT)	SIGMA, US
Ethylenediaminetetraacetic acid (EDTA) disodium salt dihydrate	SIGMA, US
GelRed Nucleic Acid Gel Stain, 10,000X in water	Biotium, US
Hydrogen tetrachloroaurate(III) hydrate, 99.9% (metals basis), Au 49% min	Alfa Aesar, US
Magnesium chloride hexahydrate	SIGMA, US
N,N,N',N'-Tetramethylethylenediamine, Electrophoresis Grade	Alfa Aesar, US
N,N'-Methylenebis(acrylamide)	SIGMA, US
PCR loading buffer	Top-Bio, CZ
Polyethylenimine, Linear, MW 2,500 (PEI 2500)	Polysciences, US
Sodium citrate tribasic dihydrate	SIGMA, US
Tris base	SIGMA, US
Tween 20, viscous liquid	SIGMA, US

## 5.2 Instruments and used software

Analytical balance BBC	Boeco, DE
Centrifuge 5430 R, rotor FA-45-24-11-HS	Eppendorf, DE
MR Hei-Tec Magnetic Stirrer with Heating	Heidolph, DE
Spectrophotometer SPECORD 250 PLUS, Software WinASPECT PLUS version 4.1.0.0	Analytik Jena, DE
Elmasonic P 60 H Ultrasonic cleaning unit	Elma, DE
Incubator INCU-Line IL10	VWR International, US
PowerPac™ Basic Power Supply	Bio-Rad Laboratories, US
Imaging System c600, software 2.1.1.0507	Azure Biosystems, US
Centrifuge 3-30 KS, Fixed-angle rotor 12110	SIGMA, US
Transmission Electron Microscope JEM-1011, Software ImageJ 1.52a	JEOL, USA
Multimode plate reader Spark, Software version 2.3	Tecan, CH
Fluoromax-4 Spectrofluorometer, Software FluorEssence version 3.5	HORIBA Scientific, JP
Zetasizer nano, Software version 7.13	Malvern Instruments, UK

## 5.3 Other materials

Automatic pipettes	Eppendorf, DE
Carbon-coated copper grids	Pyser Optics, UK
Cuvette 104 - Semi-Micro cell-QS	Hellma Analytics, DE
Cuvette Ultra-Micro Cell 105.251-QS	Hellma Analytics, DE
Laboratory glass	Simax, CZ
Microtubes	Eppendorf, DE
Mini-PROTEAN electrophoresis equipment	Bio-Rad Laboratories, US

Nunc 384-Well Optical Bottom Plate black	Thermo Fisher Scientific, US
Pipette tips	Eppendorf, DE
Quartz cuvette 26.100-F	Starna scientific, UK

## 5.4 Methods

### 5.4.1 Synthesis of gold nanoparticles

To prepare gold nanoparticles, 20 mL of Milli-Q water and 200  $\mu$ L of 1% H<sub>2</sub>AuCl<sub>4</sub> were mixed in a 60 mL vial. After adding a magnetic stir bar into the vial, the mixture was heated to 110 °C while continuously stirring. When the mixture started to boil gently, 1 mL of 1% trisodium citrate solution was added. After 15 min, the heating was turned off, and the mixture was left standing to cool down and incubated overnight at RT while stirring.

### 5.4.2 Transmission electron microscopy

The size of synthesized gold nanoparticles was determined by transmission electron microscopy (TEM) on a JEM-1011 transmission electron microscope (JEOL) operated at 80 kV. The samples were prepared for measurements following the protocol published by Rehor and Cigler<sup>44</sup>. Briefly, the carbon-coated copper grid (Pyser) was placed into a UV-ozone chamber, carbon layer up, for 15 min. Then, the grid was placed on a 0.1 mg/mL linear PEI 2500 solution droplet for 10 min. Subsequently, after drying the grid with a tissue, the grid was placed on the droplet of Milli-Q water. After 1 minute, the grid was again dried with a tissue and subsequently placed on a 10x concentrated AuNPs solution for 3 min. The AuNPs solution was then gently removed from the grid with a piece of tissue. TEM images were recorded and analyzed by Helena Raabová at IOCB, Prague.

ImageJ software was used to analyze particle size distributions. First, to remove uneven illumination, a third-order polynomial fitting was applied. Second, to remove background noise, Gaussian blur (2 pixels) filter was used. Brightness and contrast were adjusted, gray-scale images were converted into binary images and the projected areas of all particles were analyzed using the software. Average particle diameter and its standard deviation were calculated from the number distribution of 731 particles.

### 5.4.3 Dynamic light scattering

Dynamic light scattering (DLS) is the technique most commonly used to determine the size distribution profile of particles in the nanometer range. DLS provides a measurement of the Brownian motion of particles, which is related to their size.

The hydrodynamic radius of gold nanoparticles was determined using the Zetasizer Nano (Malvern Instrument). The wavelength of the source was 633 nm, and the scattering angle was 173°. Cumulant and NNLS algorithm were used to fit the autocorrelation function, which enables us to determine the diffusion coefficient of the particles and thus to calculate their hydrodynamic radius using the Stokes-Einstein equation. The synthesized solution of gold nanoparticles was measured without any dilution at 25 °C in a quartz cuvette 105.251 - Ultra-Micro cell (Hellma Analytics). The number distributions (intensity size distribution was converted into the corresponding number size distribution using the Mie theory) were fitted to lognormal curves. The values of the geometric mean and geometric standard deviation calculated from the fit were used to determine the diameter of average surface, which makes it possible to compare the mean from DLS with the mean from TEM. The Hatch-Choate conversion equation (*Eq. 7*) applicable to lognormal distributions allows us to convert any type of average diameter,  $d_x$ , from geometric mean,  $d_g$ , and geometric standard deviation,  $\sigma_g$ <sup>45</sup>. The form of Hatch-Choate conversion equation is:

$$d_x = d_g e^{b \ln^2 \sigma_g}, \quad \text{Eq. 7}$$

where  $b$  value depends on the type of average and the distribution momentum. For diameter of average surface, the  $b$  value is 1. The calculated values of the diameters of average surface were averaged, and the resulting mean values and standard deviations are displayed.

### 5.4.4 Determination of the concentration of gold nanoparticles

The concentration of gold nanoparticles was determined by measuring the absorbance at 450 nm on a 104 - Semi-Micro cell (Hellma Analytics). The value of the extinction coefficient used to calculate the concentration was chosen according to the size of nanoparticles<sup>46</sup>. For 17 nm (diameter) AuNPs, the value of extinction coefficient is:

$$\varepsilon_{450} = 3.24 * 10^8 \text{ M}^{-1} \text{ cm}^{-1}.$$

Particle concentration ( $c$ ) can be calculated from the absorption ( $A$ ) and extinction coefficient ( $\epsilon$ ) at 450 nm for a standard path length of 1 cm, according to Eq. 8:

$$c = \frac{A_{450}}{\epsilon_{450}} \quad \text{Eq. 8}$$

All samples were diluted 5x, 2x and 1x (not diluted), and the resulting absorbance values were averaged.

#### 5.4.5 Synthesis of oligonucleotide-modified gold nanoparticles

A classical method for the synthesis of oligonucleotide-modified gold nanoparticles is known as the „salt-aging method“, which is based on a slow increase in salt concentration for the attachment of oligonucleotides on a AuNP surface<sup>47</sup>. However, this method requires almost two days to complete. We thus utilized an alternative method termed „freezing method“, which allows us to obtain comparable particles via a much faster and simpler procedure<sup>48</sup>.

In total, 100  $\mu\text{L}$  of 16.7 nM (1.67 pmol) AuNPs was mixed with 6  $\mu\text{L}$  of 50  $\mu\text{M}$  DNA1a/2a/3a, if not mentioned otherwise, and placed into the  $-80^\circ\text{C}$  freezer for 30 min. After incubation, the samples naturally thawed at RT, which was followed by 5 washing steps with 1xPBS (15,000 rcf,  $4^\circ\text{C}$ , 10 min). All samples were sonicated between the washes for 3 s in a sonication bath (Elma) at 37 kHz and at  $25^\circ\text{C}$ . The resulting oligonucleotide-modified AuNPs were resuspended in 10 mM Tris with  $\text{MgCl}_2$  (final concentration 12.5 mM). The particles used to measure the positive control were synthesized according to the same procedure with 8  $\mu\text{L}$  of 50  $\mu\text{M}$  DNA3a/4.

The oligonucleotide-modified AuNPs with different DNA coverage of AuNPs were synthesized using the same “freezing-method” procedure, but with different molar ratios of DNA per AuNP.

#### 5.4.6 Determination of the amount of DNAs on the surface of gold nanoparticles

To determine the amount of DNA on the surface of AuNP, the last step of the preparation of oligonucleotide-modified AuNPs (resuspension in 10 mM Tris with  $\text{MgCl}_2$ ), was replaced with resuspension in 80  $\mu\text{L}$  of Milli-Q water. Subsequently,

the mixture was heated at 90 °C for 3 min and immediately centrifuged (50,000 rcf, 40 °C, 10 min) in pre-heated rotor at 90 °C. The heating caused the dissociation of fluorophore-labelled DNAs (DNA1a, DNA2a) from the AuNP/DNA1a/2a/3a complex. The AuNP/DNA3a complex was subsequently centrifuged. The fluorescence of the supernatant containing DNA1a and DNA2a was measured on a Tecan Spark (excitation 628 nm, emission 665 nm, 27 °C) in a Nunc 384-Well Optical Bottom Plate (Thermo Fisher Scientific) in triplicates. The measured signal was compared with the calibration curve of DNA1a and DNA2a to determine the amount of fluorophore-labelled DNAs in the sample (see Supplement S2).

To determine the precise amount of AuNPs in the sample after the washing steps, the pellet containing AuNPs with DNA3a was resuspended in Milli-Q water supplemented with trisodium citrate solution (0.05% final concentration) to the final volume of 1 mL ( $V(\text{sample})$ ) and gently sonicated. Subsequently, the absorbance at 450 nm was measured on a SPECORD 250 PLUS spectrophotometer (Analytik Jena) to calculate the amount of AuNPs in the pellet. The amount of substance of DNA in the supernatant divided by the amount of substance of AuNPs in the pellet gives the number of DNA complexes per gold nanoparticle.

#### 5.4.7 Fluorescence measurements

The vast majority of fluorescence measurements was performed on a Tecan Spark in a Nunc 384-Well Optical Bottom Plate (Thermo Fisher Scientific), if not mentioned otherwise. The volume of each sample was 25  $\mu\text{L}$  per well. To measure the signal from DNAs containing Cy3 (DNA1, DNA2), the excitation monochromator was set to 543 nm (20 nm bandwidth) and emission monochromator to 580 nm (20 nm bandwidth). DNAs containing Atto633 (DNA1a, DNA2a) were measured with excitation wavelength 628 nm (20 nm bandwidth) and emission wavelength 665 nm (20 nm bandwidth). The gain of all connected measurements was set to a constant value. The reaction progress was measured at 37 °C in duplicates, while all the other measurements were performed at 27 °C in triplicates, if not mentioned otherwise.

The initial part of the kinetic measurement (the progress of the reaction within the first hour) was performed on a HORIBA Scientific Fluoromax-4 Spectrofluorometer

for its increased sensitivity compared with that of the Tecan Spark, adjustable slit size and possibility of working in anti-photobleaching mode, which reduces the illumination of the sample by closing the shutter between individual measurements. For samples containing DNAs with Cy3 (DNA1, DNA2) the excitation monochromator was set to 546 nm (0.15 nm slit) and the emission monochromator to 575 nm (29.4 nm slit). DNAs containing Atto633 (DNA1a, DNA2a) were measured with an excitation wavelength of 625 nm (0.15 nm slit) and with an emission wavelength of 655 nm (29.4 nm slit). The monochromator settings were chosen to eliminate the photobleaching effect. All measurements were performed in anti-photobleaching mode with a detector voltage set to 950 V, in a 26.100-F quartz cuvette (Starna scientific) at 37 °C, in monoplicates. The volume of each sample in a cuvette was 120  $\mu$ L.

#### 5.4.7.1 Sample composition

The progress of the reaction (the release of fluorophore-labelled DNAs due to the presence of miRNA) was measured with final concentrations of components as outlined in *Table 1*, which describes the composition of the positive control sample as well. The sample of the negative control was the same as that using in the reaction but without DNA4 (fuel) and miRNA. The miRNA concentrations varied throughout the experiments and are specified in every measurement. All reactions were performed in 10 mM Tris buffer supplemented with 12.5 mM MgCl<sub>2</sub> and 0.01 % Tween-20.

*Table 1 Components of the samples for measurement of the reaction and positive control.*

Reaction components	c (final)	Positive control components	c (final)
DNA1/2/3 or Au/DNA1a/2a/3a	0.08 $\mu$ M	DNA3/4 or DNA3a/4	0.08 $\mu$ M
DNA4 (fuel)	0.08 $\mu$ M	DNA1 or DNA1a	0.08 $\mu$ M
		DNA2 or DNA2a	0.08 $\mu$ M

Fluorescence measurements showing the selectivity of the system when using miRNAs with one or multiple sequence mismatches were performed under the same

conditions as those used in experiments with completely complementary miRNA – let-7a. The samples containing 20 nM miRNA were incubated at 37°C for 3 hours and measured every 20 min on Tecan Spark in duplicates. The sequences of all miRNAs used in the experiments are outlined in *Table 2*.

*Table 2 Sequences of all the miRNAs used in the experiments. The single point mutations are marked in yellow.*

Name	Sequence (5'- 3')
let-7a	UGAGGUAGUAGGUUGUAUAGUU
let-7d	UGAGGUAGUAGGUUGUAU <u>G</u> GUU
let-7e	UGAGGUAG <u>G</u> AGGUUGUAUAGUU
miR-21	UAGCUUAUCAGACUGAUGUUGA

#### 5.4.8 Stability of AuNP/DNA conjugates in glutathione

Glutathione (GSH), as one of the most important low-molecular-weight antioxidants in cells, is found in the cytosol in concentrations ranging from 1 to 10 mM. However, in most cells, GSH concentration reaches 1-2 mM, whereas in hepatocytes, from where GSH is exported, its concentration reaches 10 mM<sup>49</sup>. Because GSH contains thiol group, which could potentially release DNA constructs from the surface of AuNP, the stability of AuNP/DNA in various GSH concentrations over the 24-hour period was studied. For this purpose, 30 nM AuNP/DNA was incubated at 37°C in 12.5 mM MgCl<sub>2</sub> and 0.01% Tween-20 for a given time period. Subsequently, the mixture was centrifuged down (50,000 rcf, 37°C, 10 min) to obtain a supernatant containing DNA complexes released due to the presence of GSH in solution. The fluorescence of the supernatant was measured in duplicates at 37°C on Tecan Spark with the settings presented in chapter 5.4.7.

The sample of the negative control did not contain any GSH. The sample of the positive control was heated at 90 °C for 3 min to release all fluorophore-labelled DNAs from AuNP/DNA constructs for a maximal fluorescence signal. Afterwards, the sample was centrifuged in a pre-heated rotor at 90 °C (50,000 rcf, 40 °C, 10 min), and the supernatant was measured according to the settings presented above.

## 5.4.9 DNA polyacrylamide gel electrophoresis

DNA polyacrylamide gel electrophoresis was performed to analyze reaction mixture composition after a 24-hour incubation period at 37 °C. The composition of a 15% polyacrylamide gel is outlined in *Table 3*.

*Table 3 Components for preparation of a 15% polyacrylamide gel.*

Component	Volume (μL)
10x TBE buffer	700
Milli-Q H <sub>2</sub> O	3,915
45 % acrylamide/bis-acrylamide	2,333
10 % (w/v) APS	49
TEMED	2.8

All DNA (400 nM) and RNA (500 nM) samples supplemented with 12.5 mM MgCl<sub>2</sub> were incubated for 24 hours at 37 °C.

To prepare the gel showing the sample composition of AuNP system, after incubating the samples for 24h, 15 mM DTT was added into the samples to release DNA from the AuNP surface and incubated overnight at RT. The next day, the samples containing AuNPs were centrifuged (50,000 rcf, 20°C, 10 min), and the supernatant was treated in the same way as all other samples.

Just before running the gel, the samples were mixed with 2.5 μl PCR loading buffer and loaded into the wells of the gel. The gel was run in 1x TBE buffer at 100 V for 5 min, followed by 50 V for 3 hours. Subsequently, the gel was stained with Gelred solution (100 mL of Milli-Q H<sub>2</sub>O + 3 μL 10,000x Gelred) for 30 min. Imaging system c600 (Azure Biosystems) was used for image acquisition with excitation at 302 nm and an exposure time of 1 minute. The colors of the images were inverted, and the contrast was enhanced.

## 6 RESULTS

### 6.1 Synthesis and characterization of gold nanoparticles

The gold nanoparticles were synthesized according to the protocol described in chapter 5.4.1. The solution of gold nanoparticles was analyzed to determine the size and concentration of AuNPs.

#### 6.1.1 Determination of the size of gold nanoparticles

The recorded TEM image and the processed binary image are showed in *Figure* . *Table 4* shows values from DLS measurement of AuNPs and AuNP/DNA complex – intensity-weighted harmonic mean diameter (z-average), polydispersity index (PDI), values from fitted number distributions – number-weighted geometric mean diameter ( $D_{ng}$ ) and geometric standard deviation ( $\sigma_g$ ), diameters of average surface (or number-weighted surface mean diameter,  $D_{ns}$ ) calculated using the Hatch-Choate equation (see *Eq. 7*) and the diameter of the average surface of AuNPs from TEM. *Figure* shows the number distributions from both methods, whereas *Figure* displays their cumulative curves.

*Table 4 Values from DLS and TEM measurements for AuNPs and AuNP/DNA. All values (except of PDI which is dimensionless) are expressed as nm.*

	DLS					TEM
	z-average	PDI	$D_{ng}$	$\sigma_g$	$D_{ns}$	$D_{ns}$
AuNP	$12.15 \pm 0.10$	$0.206 \pm 0.005$	$13.80 \pm 0.74$	$1.26 \pm 0.01$	$14.56 \pm 0.75$	$17.41 \pm 1.71$
AuNP/DNA	$48.08 \pm 0.52$	$0.258 \pm 0.002$	$40.05 \pm 2.89$	$1.26 \pm 0.01$	$42.31 \pm 2.91$	X

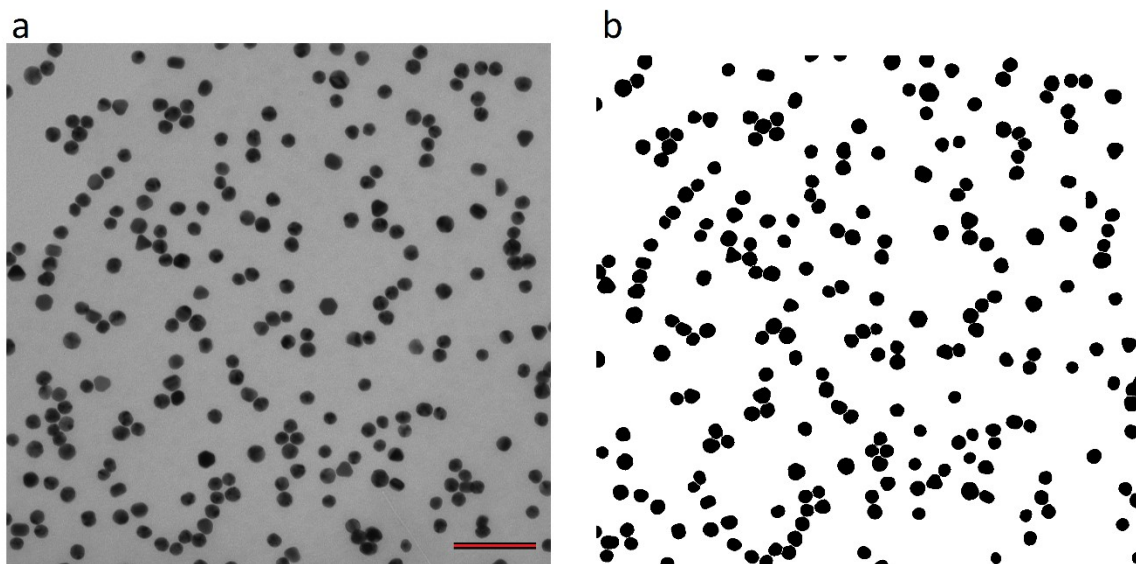


Figure 9 TEM image analysis procedure, (a) original bright-field image, (b) processed binary image; the scale bar corresponds to 100 nm.

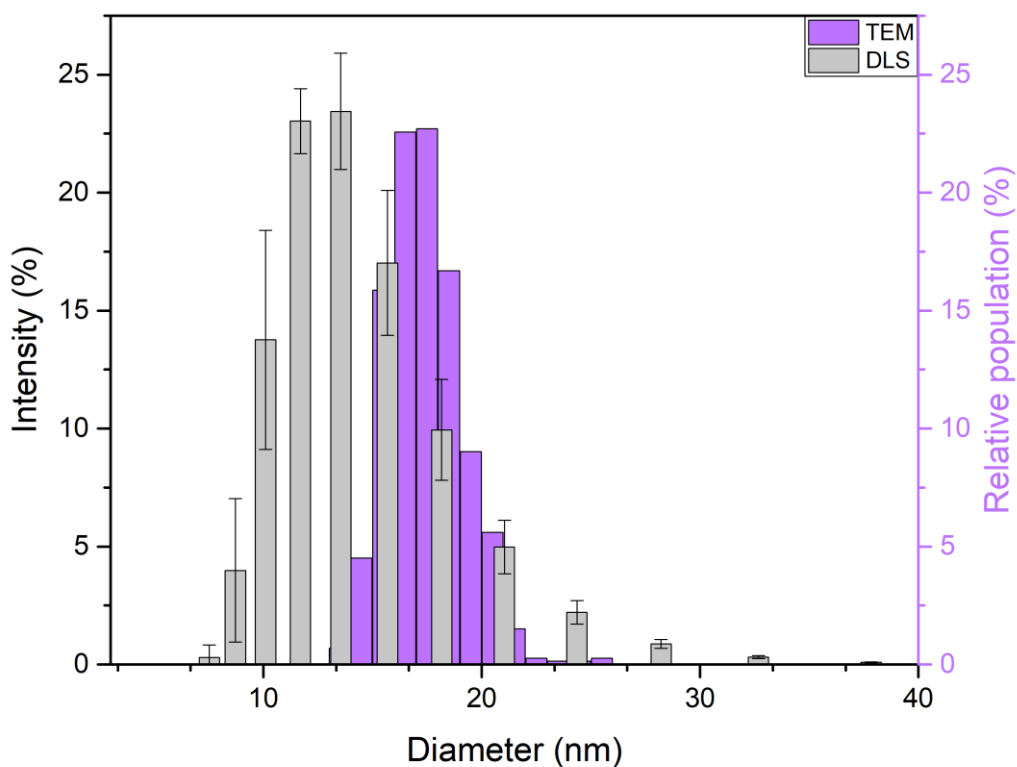


Figure 10 Number distributions from TEM and DLS of AuNPs. TEM measurements display the diameter of AuNPs, whereas DLS measurements display the hydrodynamic diameter. Error bars in the DLS distributions represent standard deviations from three measurements of the same sample.

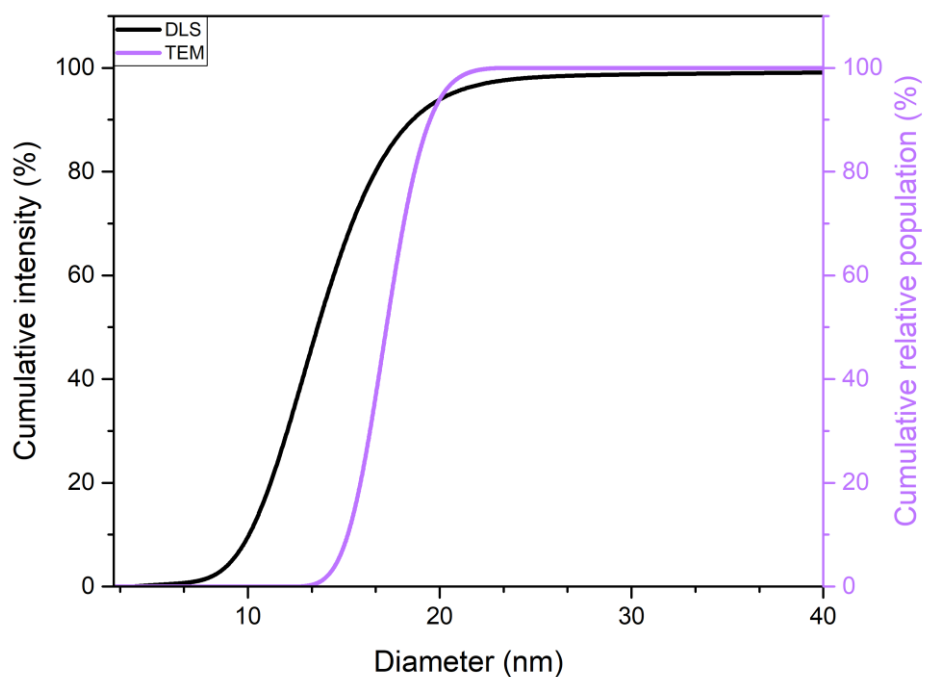


Figure 11 Cumulative curves of number distributions from TEM and DLS measurements.

## 6.2 Construction and characterization of oligonucleotide-modified gold nanoparticles

To prepare oligonucleotide-modified AuNPs, a 1.82 nM stock solution of 17 nm AuNPs was used (the details of determination of AuNPs concentration are presented in the Supplement S1). The “freezing method”<sup>48</sup> was followed to construct oligonucleotide-modified gold nanoparticles (see the chapter 5.4.5).

### 6.2.1 Determination of the number of DNA complexes per gold nanoparticle

The amount of DNA complexes per AuNP was determined following the protocol described in chapter 5.4.6. After heating and centrifugation, the fluorescence of the supernatant containing DNA1a and DNA2a was measured on Tecan Spark. The values were used to determine the concentration of DNA1a and DNA2a in the supernatant from the calibration curve of DNA1a and DNA2a (see the Supplement S2). An example of the calculations of the molar ratio 180 are shown below.

The average value of relative fluorescence from the supernatant measurement was 13,380. Using the equation of the calibration curve of DNA1a and DNA2a (see Supplement S2), the value of concentration and the amount of substance of DNA1a and DNA2a in the supernatant was determined:

$$c(\text{DNA}) = 0.436 \mu\text{M}$$

$$V(\text{supernatant}) = 89.0 \mu\text{L}$$

$$n(\text{DNA}) = c(\text{DNA}) \cdot V(\text{supernatant}) = 0.436 \cdot 10^{-6} \cdot 89.0 \cdot 10^{-6} = 3.88 \cdot 10^{-11} \text{ mol}$$

The pellet resuspended in Milli-Q water supplemented with trisodium citrate was measured on a SPECORD 250 PLUS spectrophotometer (Analytik Jena). *Figure 12* shows absorbance spectra of the initial AuNP solution used to synthesize oligonucleotide-modified AuNPs and AuNPs/DNA3a after the washing steps. Washing caused the loss of approximately 10 % nanoparticles. The value of  $A_{450}$  calculated from the spectrum of AuNPs/DNA3a after the washing steps was used in subsequent calculations of the amount of substance of AuNPs in the pellet.

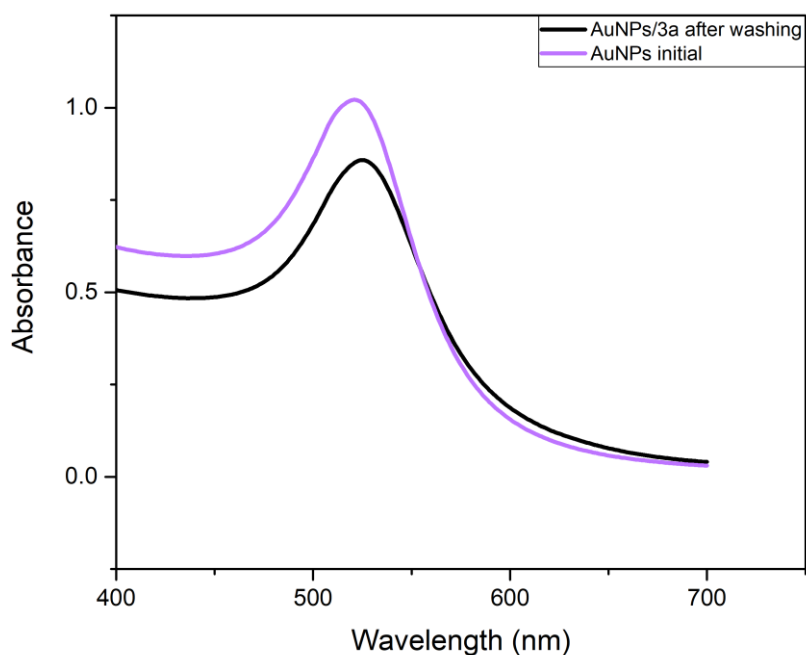


*Figure 12 Absorbance spectra of the initial solution of AuNPs used to prepare oligonucleotide-modified AuNPs and the AuNPs/DNA3a solution after 5 washing steps.*

$$n(\text{AuNPs}) = c(\text{AuNPs}) \cdot V(\text{sample}) = \frac{A_{450} \cdot V(\text{sample})}{\varepsilon_{450}} = \frac{0.4870 \cdot 1000 \cdot 10^{-6}}{3.24 \cdot 10^8} \\ = 1.50 \cdot 10^{-12} \text{ mol}$$

The amount of substance of DNA in supernatant divided by the amount of substance of AuNPs in the pellet gives the number of DNA complexes per gold nanoparticle:

$$\frac{n(\text{DNA})}{n(\text{AuNPs})} = \frac{3.88 \cdot 10^{-11}}{1.50 \cdot 10^{-12}} = 25$$

The values of absorbance and fluorescence measured in samples prepared with different ratios of DNA per AuNP and all calculated values are displayed in *Table 5*.

*Table 5 Measured and calculated values for AuNPs with different DNA coverage density*

$n_{\text{DNA}}/n_{\text{AuNP}}$ initial	RFU	$c_{\text{DNA}}$ ( $\mu\text{M}$ )	$n_{\text{DNA}}$ (pmol)	$A_{450}$	$n_{\text{AuNP}}$ (pmol)	DNAs per AuNP
180	13,380	0.436	38.8	0.4870	1.5	25
150	13,068	0.426	34.9	0.4838	1.5	23
120	12,513	0.407	31.7	0.4521	1.4	22
90	8,712	0.282	22.1	0.3576	1.1	20

## 6.2.2 Comparison of reaction yields for AuNPs with different DNA coverage density

In parallel with the sample preparation described above, samples prepared to compare reaction yields with AuNPs with different DNA coverage density were synthesized according to the same procedure up to the point of resuspension after the washing steps. These samples were resuspended in 10 mM Tris supplemented with  $\text{MgCl}_2$  (final concentration 12.5 mM).

The samples prepared to compare reaction yields were prepared according to the *Table 1* with 0.1  $\mu\text{M}$  let-7a. These samples were incubated for 24 hours at 37 °C and subsequently measured on Tecan Spark with settings presented in chapter 5.4.7. *Figure 13* shows the difference between the values of relative fluorescence of the reaction mixture and the negative control for AuNPs with different DNA coverage density and the amount

of DNAs per AuNP as a function of the initial ratio of DNA per AuNP used during the synthesis of oligonucleotide-modified gold nanoparticles.

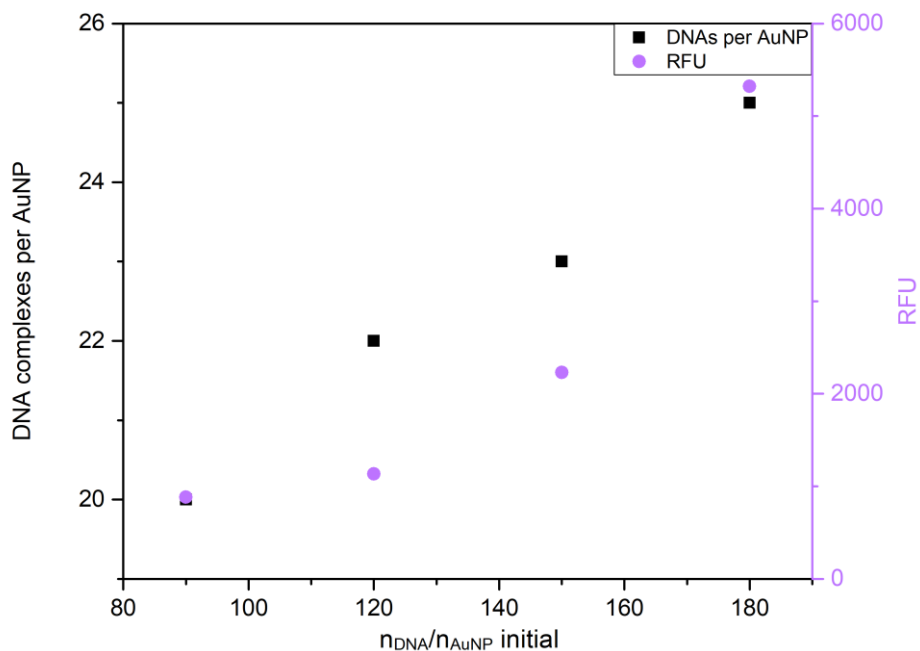


Figure 13 Representation of relative fluorescence and the amount of DNA complexes per AuNP as a function of the initial DNA/AuNP ratio used to prepare oligonucleotide-modified AuNPs.

As the signal was the strongest when the DNA coverage was the highest, all subsequent experiments were performed with AuNPs with maximal DNA coverage (i.e. 25 DNA complexes per AuNP). The AuNP/DNA conjugates designated for the subsequent measurements were prepared in exactly the same way, and the concentration of DNA complexes in this sample was 1.6  $\mu$ M.

### 6.3 Measurements of the progress of the reaction

The reaction mixture was prepared according to *Table 1*. Three different concentrations of miRNA (let-7a) were tested – 20 nM, 100 nM and 300 nM. In every single time point, the negative and positive control were measured as well. *Figure* shows the reaction yields of the process of fluorophore-labelled DNA release due to the presence

of various concentrations of let-7a in the reaction mixture for the system containing gold nanoparticles and an analogous system without them. To show the stability of AuNP/DNA, the size of this construct was measured during the 7-day period (see Supplement S4).

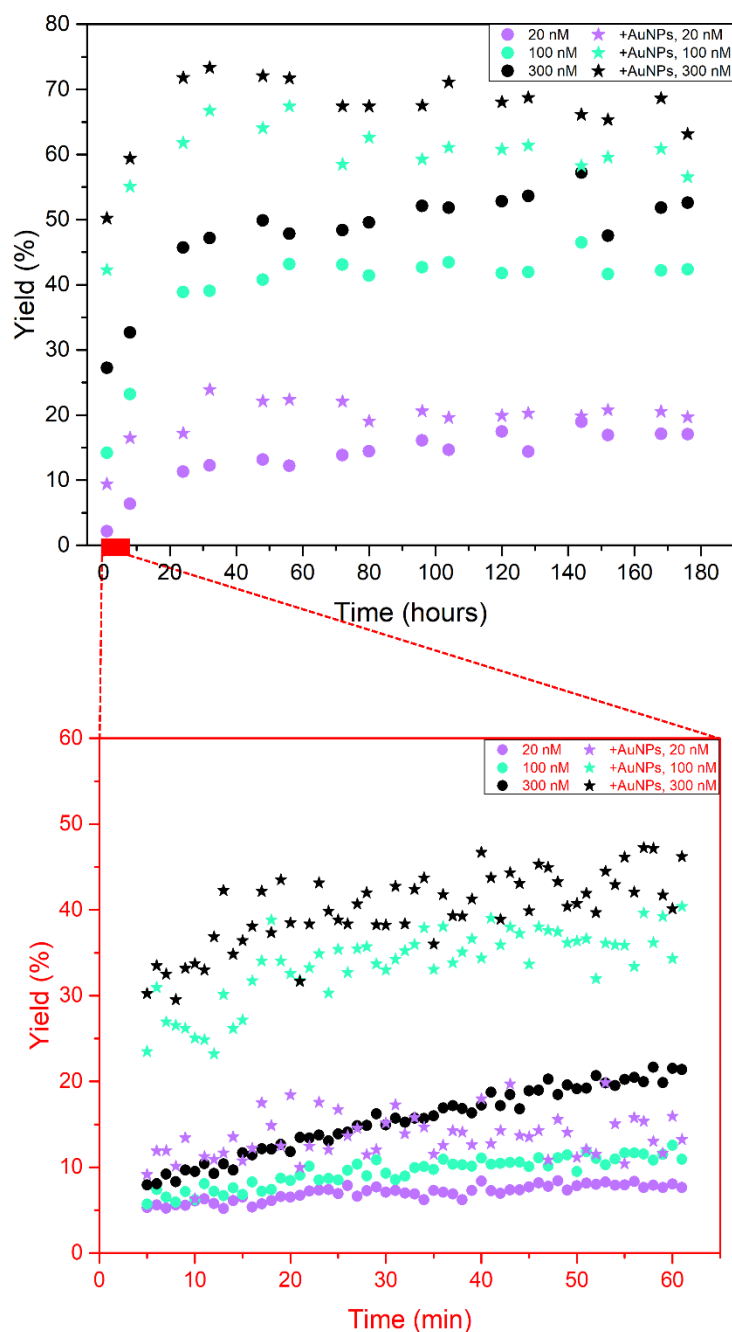
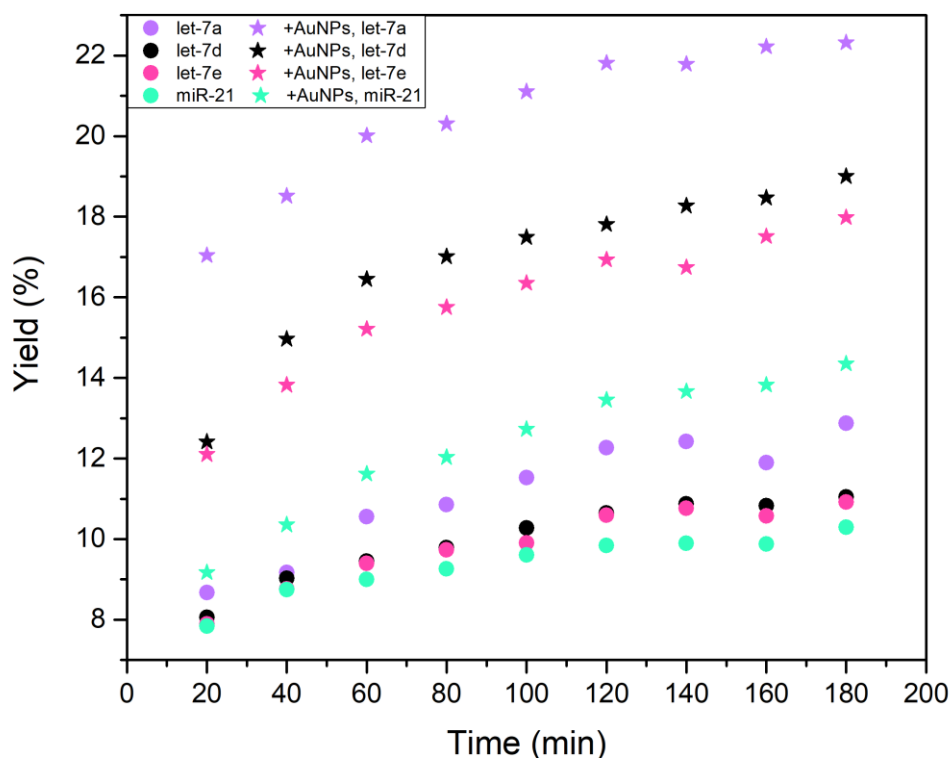


Figure 14 Representation of the reaction yields of the process of fluorophore-labelled DNA release due to the presence of different concentrations of let-7a in several time points.

### 6.3.1 Selectivity to various miRNAs

The reaction mixture was prepared according to *Table 1* with 20 nM miRNAs of different sequences (see *Table 2*) and incubated at 37 °C for 3 hours. *Figure 15* shows the reaction yields of the process of fluorophore-labelled DNA release due to the presence of completely complementary miRNA (let-7a), one base mismatch miRNA (let-7d and let-7e) and random miRNA (miR-21) for DNA and AuNP/DNA systems.



*Figure 15* Selectivity of DNA and AuNP/DNA system to various miRNAs.

### 6.4 Stability of AuNP/DNA in GSH environment

*Figure 16* displays the stability of AuNP/DNA constructs expressed as percentage of released DNA complexes from AuNP surface due to the presence of 2, 6 or 10 mM GSH over a 24-hour period. The concentration of 14 mM GSH was also tested but caused immediate aggregation of AuNP/DNA.

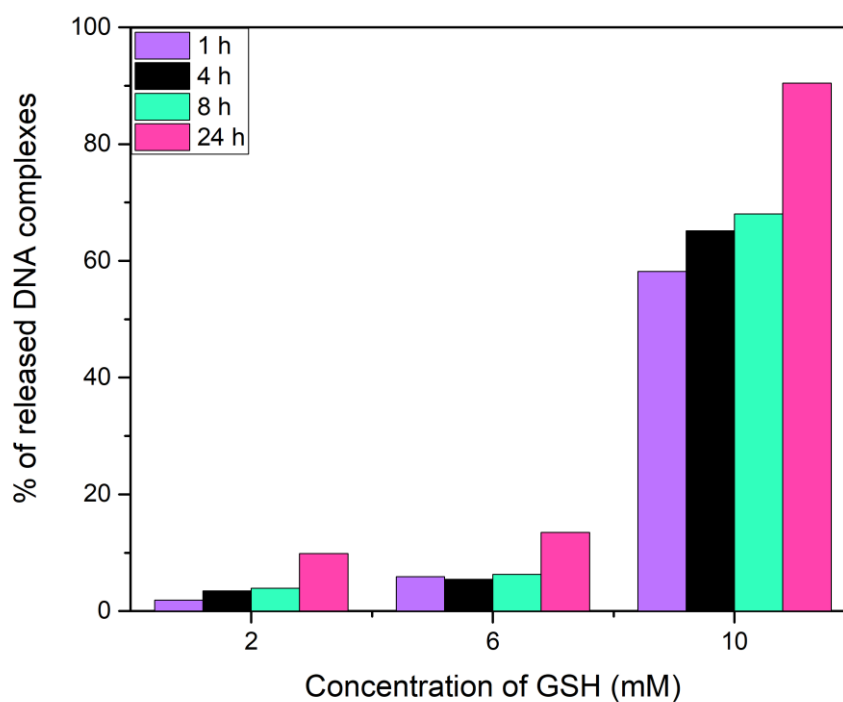
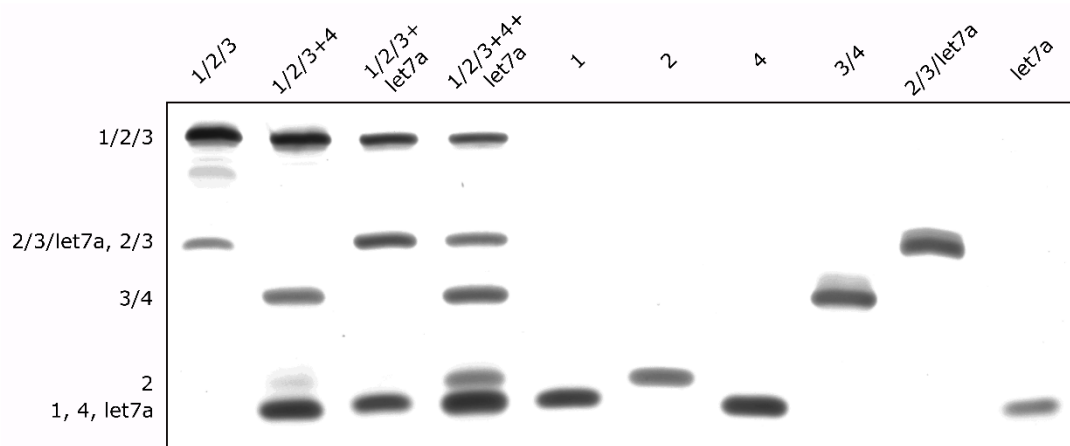


*Figure 16 Stability of AuNP/DNA constructs in various GSH concentrations over one day period.*

## 6.5 Reaction mixture composition (DNA electrophoresis)

Images of the gels showing the composition of the reaction mixture for the AuNP/DNA and the analogous DNA systems are displayed in *Figure 17*.

a



b

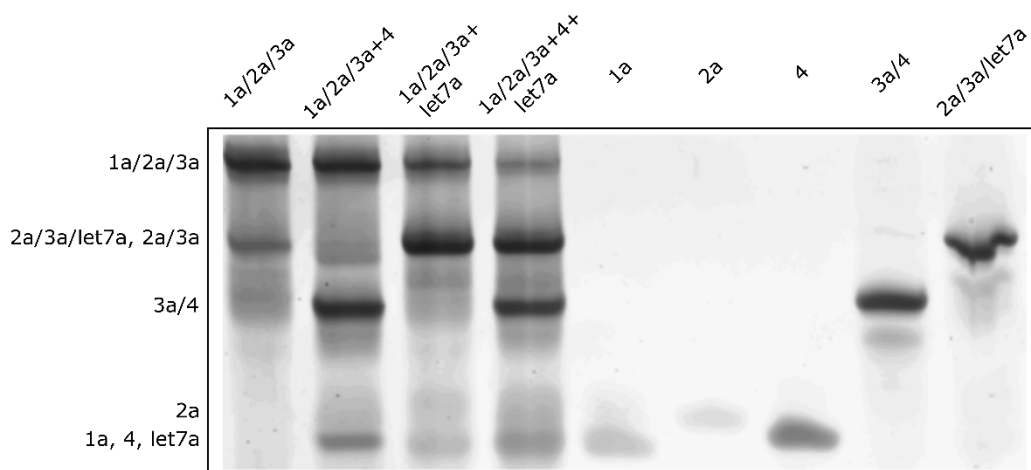


Figure 17 Polyacrylamide gels showing the composition of the reaction mixture for the (a) DNA and (b) analogous AuNP/DNA detection systems.

## 7 DISCUSSION

The size of the AuNPs synthesized in this study was assessed using two different methods – TEM and DLS. TEM showed that the number-weighted surface mean diameter of AuNPs was  $17.41 \pm 1.71$  nm, whereas the hydrodynamic number-weighted surface mean diameter calculated from DLS measurement was  $14.56 \pm 0.75$  nm (see *Table 4*). This difference is caused by the nature of both methods and by the corresponding statistics of the measurements. Each measuring technology sees the particles through different weighting factors. TEM measures the particles based on their number, whereas DLS detects the intensity of light scattered by particles based on their volume. For this reason, the measured values must be converted into the same base when comparing the results from two different measuring technologies<sup>50</sup>. Furthermore, the diameter of AuNPs using TEM was calculated from 731 particles, whereas the number of particles contributing to the determination of the hydrodynamic diameter from DLS is several orders of magnitude higher. All these factors can cause slight discrepancies when measuring the size of AuNPs from DLS and TEM, even upon conversions, which allow us to compare values from different measuring technologies.

The hydrodynamic number-weighted surface mean diameter of the AuNP/DNA construct reaches  $42.31 \pm 2.91$  nm in contrast to  $14.56 \pm 0.75$  nm of uncoated AuNPs (see Supplement S3). These results confirm that the DNA coating is present on the AuNP surface with an approximate thickness of 14 nm, in line with the expected value – DNA3a is composed of 60 base pairs (center-to-center distance between neighboring nucleotides is  $0.34$  nm<sup>51</sup>), so its length reaches approximately 20 nm. This slight discrepancy may be caused by the DNA structure, which is not fully extended, and by the transformations that were applied to assess the number-weighted surface mean diameter.

Determining the number of DNA complexes per gold nanoparticle allowed us to calculate the concentration of DNA complexes and AuNPs in solution. After mixing AuNPs with DNA complexes to prepare oligonucleotide-modified AuNPs using the “freezing method” and subsequently dissociate fluorophore-labelled DNAs from the DNA structure, a 4 nm red shift of the 520 nm plasmon peak was observed in the absorbance spectra (see *Figure 12*). This can be attributed to DNA present on the surface of the AuNP, which changes the local dielectric constant and thus the localized surface plasmon resonance effect.

AuNPs with varying DNA coverage were prepared to compare the kinetics of the reaction to show whether and the extent to which the rate of the reaction is affected by DNA coverage. The AuNP/DNA constructs were stable during the 7-day measurement, as confirmed by DLS measurements (see Supplement S4). Fluorescence measurements thus allowed us to compare these constructs and showed that the higher the DNA coverage density is, the faster the release of fluorophore-labelled DNAs will be due to the presence of miRNA in the solution. These results led us to use the construct with maximal DNA coverage (i.e. 25 DNA complexes per AuNP) in all subsequent experiments.

The measurements of the fluorescence signal caused by the release of fluorophore-labelled DNAs from DNA complexes due to the presence of different concentrations of miRNA (let-7a) in solution allowed us to compare the kinetics of this process when using the AuNP/DNA structure and an analogous DNA structure with intramolecular quenchers (see *Figure 14*). The yield of the reaction is higher when using AuNPs than the analogous structure with intramolecular quenchers in the DNA sequence for all let-7a concentrations, in every single time point. After the 60-minute incubation, for 300 nM let-7a, the AuNP/DNA construct reaches a yield of 46 %, whereas the yield reached with the DNA construct is only 21 %. For 100 nM let-7a, the AuNP/DNA construct provides a 40 % yield, versus 11 % with the DNA system. Taken together, after 60 min, the reaction yield of the AuNP/DNA system is more than 2 times higher than that of the DNA system without AuNPs and thus provides a much stronger fluorescence signal. This trend is maintained throughout the 7-day measurement because AuNPs make it possible to group a large number of DNA complexes. When the miRNA meets the toehold region on the DNA complex present in AuNP, it quickly displaces both fluorophore-labelled DNAs (DNA1a, DNA2a) and is finally displaced itself by DNA fuel (DNA4). The released miRNA is already in the proximity of the neighboring DNA complex present on the AuNP and does not have to diffuse through the solution to meet another DNA complex. This effect of locally increased DNA concentration provided by AuNPs and the cascade nature of this system significantly accelerate the overall process of miRNA detection in the solution. The difference in final reaction yields can be attributed to the different nature of both systems. As a result, the chemical equilibrium is reached at different points. These fluorescence measurements provide detailed information about the reaction yields of both systems in several time points, which unfortunately has not been mentioned in the previous

work on the purely DNA system<sup>43</sup>, wherein only relative values without positive control were displayed.

Selectivity measurements to various miRNAs were performed with 4 miRNAs – completely complementary let-7a, let-7d with one base mismatch in toehold sequence, let-7e with one base mismatch out of the toehold sequence, and random miR-21 (see *Table 2*). *Figure 15* displaying reaction yields for DNA and AuNP/DNA system shows that both systems are the most selective to completely complementary let-7a and the least selective to random miR-21. MiRNAs containing one base mismatch (let-7d and let-7e) are positioned between these reaction yield values.

Knowing the time point where the system is the most selective (i.e., where the difference in reaction yields for various miRNAs is the most significant) is important for future *in vitro* experiments. *Figure 15* shows that the AuNP/DNA system is the most selective after a 20-minute incubation, with 1.5-2 times higher selectivity than the DNA system, whereas the DNA system shows the lowest selectivity of all measured time points. These data also support the results mentioned above, that is, the reaction on AuNPs is much faster than in the case of the analogous DNA system. For the DNA system, the reaction progresses slowly in time, and it has not sufficiently progressed to observe any significant difference in reaction yields for various miRNAs after 20 min. The reaction on AuNPs is in full progress after 20 min. The selectivity is expected to further decrease as the reaction yields will eventually reach the same value for all tested miRNAs, when incubated for sufficiently long time periods. Taken together, the highest selectivity of the AuNP/DNA system is obtained within the first 20 min of incubation, thus suggesting that the fluorescence signal in cellular experiments should be observed shortly after the nanoparticles reach the cytosol. This will require further investigation on nanoparticle uptake kinetics and on time-dependent cellular localization of AuNP/DNA constructs.

Experiments with different concentrations of GSH were performed to ensure that the AuNP/DNA constructs would be stable in the cellular environment. *Figure 16* shows that DNA complexes are quickly displaced from the AuNP surface by high GSH concentrations (i.e. 10 mM), whereas only 10 % of DNA complexes are displaced after 24-hour incubation with 2 mM GSH, which is the concentration found in most cells. In cellular experiments, the cells are usually observed after 4 hour incubation with DNA-coated AuNPs based on the literature<sup>38,39</sup> - in this time scale, the effects of GSH on AuNP/DNA constructs are negligible at both 2 and 6 mM GSH. AuNP/DNA constructs can be thus used in most

cell types. In turn, these results also show that the use of these AuNP/DNA constructs would not be possible in high GSH environments (e.g., hepatocytes and oocytes).

Non-denaturing DNA electrophoresis allowed us to show the reaction mixture composition during the process of miRNA detection by a ternary DNA complex. *Figure 17 (a)* shows the gel with the DNA structure containing intramolecular quenchers in DNA 3 sequence. Lane 1/2/3 contains ternary DNA complex and additional duplex DNA2/3 present because of a slight difference in DNA concentrations from the exact equimolar ratio in the stock solutions. Lane 1/2/3+4 contains in addition DNA 4 (the “fuel”), which does not initiate any strand displacement because the toehold for DNA4 is hidden without miRNA (see *Figure 7*). Duplex structure DNA3/4 and single-stranded DNA2 are present again due to the non-precise equimolarity of DNA1,2,3 – DNA2 is displaced from DNA2/3 by DNA4 because it has a higher number of common base pairs with DNA3 than DNA4. The lane 1/2/3+let7a shows that the process of strand displacement was initiated. However, the cycle is stopped with intermediate 2/3/let7a due to the lack of DNA4 which displaces the second fluorophore-labelled DNA2 and subsequently let-7a, which continues to displace other DNA1. When all components are present in the reaction mixture (DNA1/2/3, DNA4, let-7a), both fluorophore-labelled DNAs are displaced, and we can observe the intermediate (2/3/let7a) and the final waste product of the reaction (3/4). *Figure 17 (b)* shows the same process for AuNPs instead of DNA with intramolecular quenchers. The resolution of the bands worsens due to the presence of DTT and residues of AuNPs in the samples. All bands in the gel are analogous to those found in the gel showing purely DNA structures. This result confirms the mechanistic similarity of the cascade reaction proceeding on both DNA and AuNP structures.

## 8 CONCLUSION

In this work, two similar detection systems based on isothermal cascade amplification were compared – the AuNP/DNA system and an analogous DNA system without AuNPs. In this thesis:

- $14.56 \pm 0.75$  nm AuNPs were synthesized
- $42.31 \pm 2.91$  nm AuNP/DNA constructs were prepared using the „freezing method“
- fluorescence measurements showed that the AuNP/DNA system provides up to 2 times higher reaction yields than the analogous DNA system
- the systems showed higher selectivity to fully complementary miRNA than miRNAs with one or multiple base mismatches
- The AuNP/DNA system provides up to 2 times higher selectivity to various miRNAs than the analogous DNA system
- AuNP/DNA constructs are stable up to 6 mM GSH
- DNA electrophoresis uncovered the mechanistic details of the fluorophore-labelled DNA release due to the presence of miRNA

Future *in vitro* experiments will be focused on the development of a photolabile spacer between the AuNP/DNA complex and DNA4 fuel which will aim to avoid the need for transfecting DNA4 separately into the cells. Moreover, the sensitivity of AuNP/DNA construct will be further tested in a wider range of miRNA concentrations. The AuNP/DNA construct will also be modified to provide a more stable construct in high-glutathione environments, which destabilizes the Au-S based constructs. Overall, the described nanosystem significantly improves the current isothermal amplification approaches for nucleic acids operating under physiological conditions. This new selective tool may be useful for miRNA detection in living cells, which will be the subject of future studies.

## 9 SUPPLEMENTS

### S1 Determination of the concentration of gold nanoparticles

The concentration of the AuNPs was calculated according to *Eq. 8* (see chapter 5.4.4). The absorbance of the samples is outlined in *Table 6*.

*Table 6 Values of absorbance at 450 nm for differently diluted samples of AuNP.*

Dilution	A <sub>450</sub>	Recalculated 1x dilution	Average A <sub>450</sub>
1x	0.5825	0.5825	0.5886
2x	0.2947	0.5894	
5x	0.1188	0.5940	

The value of the extinction coefficient at 450 nm for 17 nm AuNPs<sup>46</sup>:

$$\epsilon_{450} = 3.24 * 10^8 \text{ M}^{-1}\text{cm}^{-1}.$$

The concentration of the gold nanoparticles, calculated according to *Eq. 8*:

$$c(\text{AuNPs}) = \frac{A_{450}}{\epsilon_{450}} = \frac{0.5886}{3.24 * 10^8} = 1.82 \text{ nM}$$

### S2 Calibration curve for DNA1a and DNA2a

The calibration curve of the mixture of DNA1a and DNA2a (see *Figure 18*) was used to determine the amount of DNA per one gold nanoparticle.

The relative fluorescence of samples with different concentrations of DNA1a and DNA2a was measured. The values used to construct the calibration curve are shown in *Table 7*.

Table 7 The values of relative fluorescence of samples containing different amounts of DNA1a and DNA2a and their standard deviations.

c <sub>DNA</sub> (uM)	RFU	Standard deviation
1.875	51,476	817
1.500	42,586	1,523
0.938	28,804	251
0.750	23,462	237
0.563	17,057	293
0.375	11,813	208
0.188	7,308	242
0.000	170	4

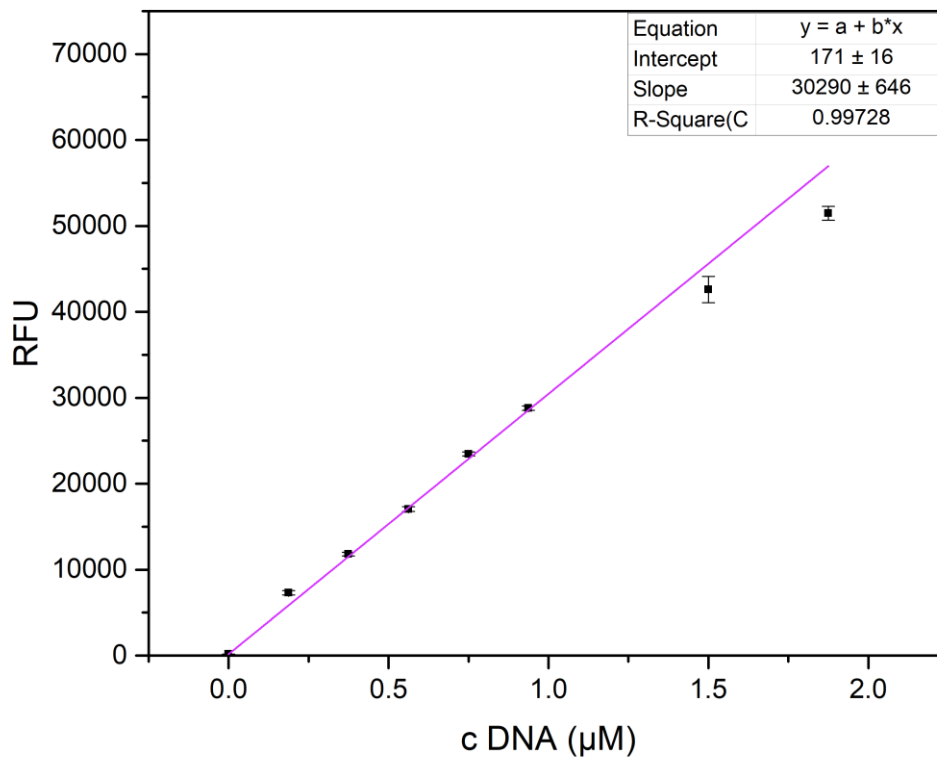


Figure 18 Calibration curve of the mixture of DNA1a and DNA2a.

Equation of the calibration curve:

$$y = 30290x + 171.$$

### S3 Comparison of AuNP/DNA and AuNP size

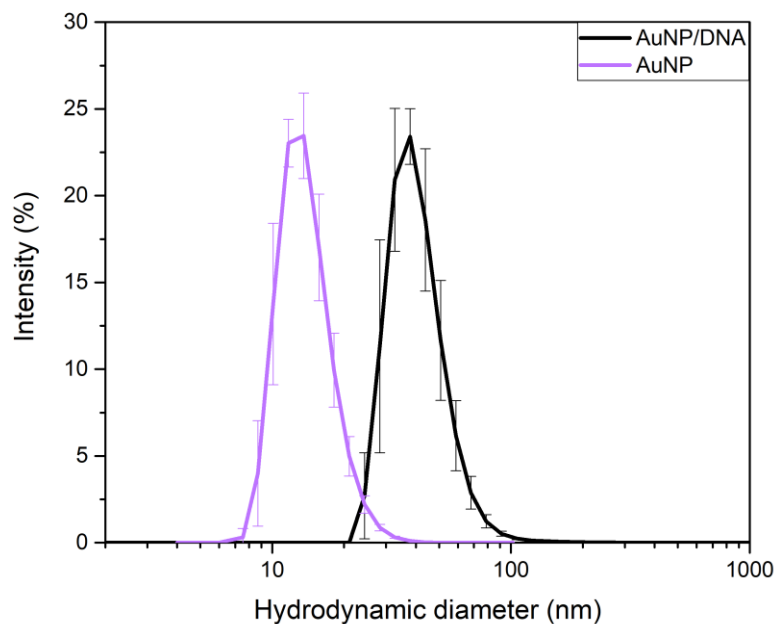


Figure 19 Number distributions of the AuNP/1/2/3a construct and AuNPs. Error bars represent standard deviations obtained from three measurements of the same sample.

### S4 Stability of AuNP/DNA complex in reaction medium

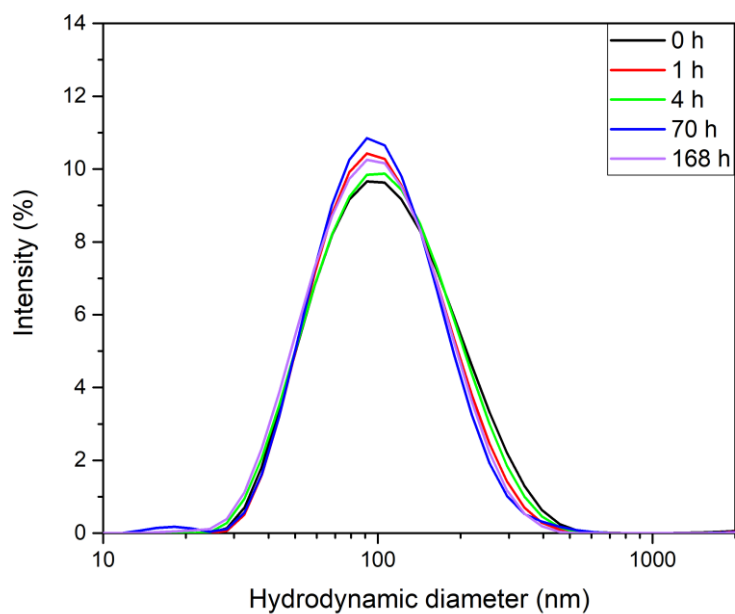
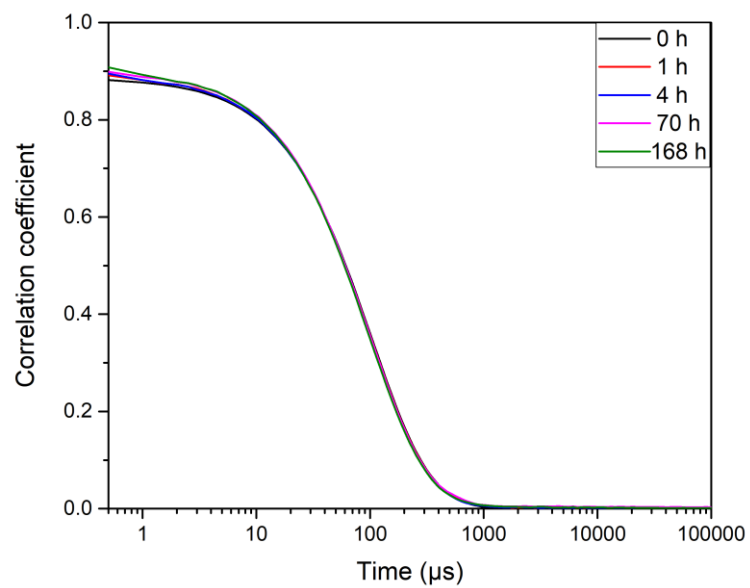


Figure 20 Intensity distributions of the AuNP/DNA1/2/3a complex in the reaction medium over a 7-day period.



*Figure 21 DLS autocorrelation functions of AuNP/DNA1/2/3a sample in reaction medium over a 7-day period.*

## 10 REFERENCES

1. Zhao, D., Yin, Q., Chang, Y. & Liu, M. Nucleic acid circuits for cell imaging: From the test tube to the cell. *TrAC - Trends Anal. Chem.* **122**, (2020).
2. Yang, Y., Zhong, S., Wang, K. & Huang, J. Gold nanoparticle based fluorescent oligonucleotide probes for imaging and therapy in living systems. *Analyst* **144**, 1052–1072 (2019).
3. Fabian, M. & Sonenberg, N. The mechanics of miRNA-mediated gene silencing: A look under the hood of miRISC. *Nat. Struct. Mol. Biol.* **19**, 586–593 (2012).
4. Ardekani, A. & Naeini, M. The role of microRNAs in human diseases. *Avicenna J. Med. Biotechnol.* **2**, 161–179 (2010).
5. Svoboda, P. A toolbox for miRNA analysis. *FEBS Lett.* **589**, 1694–1701 (2015).
6. Simmel, F., Yurke, B. & Singh, H. Principles and Applications of Nucleic Acid Strand Displacement Reactions. *Chem. Rev.* **119**, 6326–6369 (2019).
7. Chidchob, P. & Sleiman, H. Recent advances in DNA nanotechnology. *Curr. Opin. Chem. Biol.* **46**, 63–70 (2018).
8. DeVoe, H. *Thermodynamics and Chemistry*. (2001).
9. Dimitrov, R. & Zuker, M. Prediction of hybridization and melting for double-stranded nucleic acids. *Biophys. J.* **87**, 215–226 (2004).
10. SantaLucia, J., Allawi, H. & Seneviratne, P. Improved Nearest-Neighbor Parameters for Predicting DNA Duplex Stability. *Biochemistry* **35**, 3555–3562 (1996).
11. SantaLucia, J. A unified view of polymer, dumbbell, and oligonucleotide DNA nearest-neighbor thermodynamics. *Proc. Natl. Acad. Sci. U. S. A.* **95**, 1460–1465 (1998).
12. Bi, S., Yue, S. & Zhang, S. Hybridization chain reaction: A versatile molecular tool for biosensing, bioimaging, and biomedicine. *Chem. Soc. Rev.* **46**, 4281–4298 (2017).
13. Zhang, D., Turberfield, A., Yurke, B. & Winfree, E. Engineering entropy-driven reactions and networks catalyzed by DNA. *Science (80-. )*. **318**, 1121–1125 (2007).
14. Brenner, S. & Miller, J. *Encyclopedia of Genetics*. (2001).

15. Yan Shan, A. *Engineering a Robust DNA Circuit for the Direct Detection of Biomolecular Interactions*. (Springer Singapore, 2018). doi:10.1007/978-981-13-2188-7.
16. Yurke, B., Turberfield, A., Mills, A., Simmel, F. & Neumann, J. ADNA-fuelled molecular machine made of DNA. *J. Am. Chem. Soc.* **128**, 10092–10102 (2006).
17. Zhang, D. & Seelig, G. Dynamic DNA nanotechnology using strand-displacement reactions. *Nat. Chem.* **3**, 103–113 (2011).
18. Srinivas, N. *et al.* On the biophysics and kinetics of toehold-mediated DNA strand displacement. *Nucleic Acids Res.* **41**, 10641–10658 (2013).
19. Jung, C. & Ellington, A. Diagnostic applications of nucleic acid circuits. *Acc. Chem. Res.* **47**, 1825–1835 (2014).
20. Jiang, Y., Bhadra, S., Li, B. & Ellington, A. Mismatches Improve the Performance of Strand-Displacement Nucleic Acid Circuits. *Angew. Chemie* **126**, 1876–1879 (2014).
21. Liang, C. *et al.* Rational Engineering of a Dynamic, Entropy-Driven DNA Nanomachine for Intracellular MicroRNA Imaging. *Angew. Chemie - Int. Ed.* **56**, 9077–9081 (2017).
22. Lv, Y. *et al.* Entropy Beacon: A Hairpin-Free DNA Amplification Strategy for Efficient Detection of Nucleic Acids. *Anal. Chem.* **87**, 11714–11720 (2015).
23. Eckhoff, G., Codrea, V., Ellington, A. & Chen, X. Beyond allostery: Catalytic regulation of a deoxyribozyme through an entropy-driven DNA amplifier. *J. Syst. Chem.* **1**, 1–6 (2013).
24. He, L. *et al.* mRNA-Initiated, Three-Dimensional DNA Amplifier Able to Function inside Living Cells. *J. Am. Chem. Soc.* **140**, 258–263 (2018).
25. Wang, S. *et al.* Functional Titanium Carbide MXenes-Loaded Entropy-Driven RNA Explorer for Long Noncoding RNA PCA3 Imaging in Live Cells. *Anal. Chem.* **91**, 8622–8629 (2019).
26. Ou, S. *et al.* Rapid and ultrasensitive detection of microRNA based on strand displacement amplification-mediated entropy-driven circuit reaction. *Sensors Actuators, B Chem.* **255**, 3057–3063 (2018).
27. He, X., Zeng, T., Li, Z., Wang, G. & Ma, N. Catalytic Molecular Imaging of

- MicroRNA in Living Cells by DNA-Programmed Nanoparticle Disassembly. *Angew. Chemie - Int. Ed.* **55**, 3073–3076 (2016).
28. Crisalli, P. & Kool, E. Multi-path quenchers: Efficient quenching of common fluorophores. *Bioconjug. Chem.* **22**, 2345–2354 (2011).
  29. Seelig, J. *et al.* Nanoparticle-induced fluorescence lifetime modification as nanoscopic ruler: Demonstration at the single molecule level. *Nano Lett.* **7**, 685–689 (2007).
  30. Lakowicz, J. *Principles of Fluorescence Spectroscopy.* (2006).
  31. Kang, K., Wang, J., Jasinski, J. & Achilefu, S. Fluorescence Manipulation by Gold Nanoparticles: From Complete Quenching to Extensive Enhancement. *J. Nanobiotechnology* **9**, 1–13 (2011).
  32. Swierczewska, M., Lee, S. & Chen, X. The design and application of fluorophore-gold nanoparticle activatable probes. *Phys. Chem. Chem. Phys.* **13**, 9929–9941 (2011).
  33. Zhao, F. *et al.* Cellular uptake, intracellular trafficking, and cytotoxicity of nanomaterials. *Small* **7**, 1322–1337 (2011).
  34. Giljohann, D. *et al.* Oligonucleotide loading determines cellular uptake of DNA-modified gold nanoparticles. *Nano Lett.* **7**, 3818–3821 (2007).
  35. Lajoie, P. & Nabi, I. *Lipid rafts, caveolae, and their endocytosis. International Review of Cell and Molecular Biology* vol. 282 (2010).
  36. Kou, L., Sun, J., Zhai, Y. & He, Z. The endocytosis and intracellular fate of nanomedicines: Implication for rational design. *Asian J. Pharm. Sci.* **8**, 1–10 (2013).
  37. Choi, C., Hao, L., Narayan, S., Auyeung, E. & Mirkin, C. Mechanism for the endocytosis of spherical nucleic acid nanoparticle conjugates. *Proc. Natl. Acad. Sci. U. S. A.* **110**, 7625–7630 (2013).
  38. Ding, Y. *et al.* Gold nanoparticles for nucleic acid delivery. *Mol. Ther.* **22**, 1075–1083 (2014).
  39. Massich, M. *et al.* Regulating Immune Response Using Polyvalent Nucleic Acid-Gold Nanoparticle Conjugates. *Mol. Pharm.* **12**, 662–668 (2009).
  40. Seferos, D., Prigodich, A., Giljohann, D., Patel, P. & Mirkin, C. Polyvalent DNA nanoparticle conjugates stabilize nucleic acids. *Nano Lett.* **9**, 308–311 (2009).

41. Massich, M., Giljohann, D., Schmucker, A., Patel, P. & Mirkin, C. Cellular response of polyvalent oligonucleotide - Gold nanoparticle conjugates. *ACS Nano* **4**, 5641–5646 (2010).
42. Seferos, D., Giljohann, D., Hill, H., Prigodich, A. & Mirkin, C. Nano-flares: Probes for transfection and mRNA detection in living cells. *J. Am. Chem. Soc.* **129**, 15477–15479 (2007).
43. Zhang, K., Wang, K., Zhu, X. & Xie, M. Entropy-driven reactions in living cells for assay let-7a microRNA. *Anal. Chim. Acta* **949**, 53–58 (2017).
44. Rehor, I. & Cigler, P. Precise estimation of HPHT nanodiamond size distribution based on transmission electron microscopy image analysis. *Diam. Relat. Mater.* **46**, 21–24 (2014).
45. Zhang, Y. *Indoor Air Quality Engineering*. (2004). doi:10.1201/b12485.
46. Haiss, W., Thanh, N., Aveyard, J. & Fernig, D. Determination of size and concentration of gold nanoparticles from UV-Vis spectra. *Anal. Chem.* **79**, 4215–4221 (2007).
47. Cutler, J., Auyeung, E. & Mirkin, C. Spherical nucleic acids. *J. Am. Chem. Soc.* **134**, 1376–1391 (2012).
48. Liu, B. & Liu, J. Freezing Directed Construction of Bio/Nano Interfaces: Reagentless Conjugation, Denser Spherical Nucleic Acids, and Better Nanoflares. *J. Am. Chem. Soc.* **139**, 9471–9474 (2017).
49. Forman, H., Zhang, H. & Rinna, A. Glutathione: Overview of its protective roles, measurement, and biosynthesis. *Mol. Aspects Med.* **30**, 1–12 (2009).
50. Xu, R. *Particle Characterization: Light Scattering Methods*. (2000).
51. Alberts, B. *et al. Molecular Biology of the Cell*. (2014).